

1
2
3
4
5
6
7
8
9
10 **High precision registration between zebrafish brain atlases**
11 **using symmetric diffeomorphic normalization**
12
13
14
15
16
17
18
19
20
21

22 Gregory D. Marquart^{1,2}, Kathryn M. Tabor¹, Eric J. Horstick¹, Mary Brown¹,
23 Alexandra K. Geoca¹, Nicholas F. Polys³, Damian Dalle Nogare¹ and Harold A. Burgess^{1*}
24
25
26
27
28
29
30
31
32
33
34
35
36

37 ¹ Division of Developmental Biology, *Eunice Kennedy Shriver* National Institute of Child Health
38 and Human Development, Bethesda, MD 20892

39 ² Neuroscience and Cognitive Science Program, University of Maryland, College Park, MD
40 20742

41 ³ Advanced Research Computing, Department of Computer Science, Virginia Polytechnic
42 Institute and State University, Blacksburg, VA 24061

43
44
45
46
47
48
49 * Contact: burgessha@mail.nih.gov ; 301-402-6018
50
51
52
53

54 Running title: High fidelity inter-atlas registration using ANTs SyN transform

55 Keywords: zebrafish, atlas, ANTs, SyN, registration, diffeomorphism, normalization, brain
56 imaging, transgenic, virtual reality, Unity, X3D
57
58
59
60
61

Abstract

Atlases provide a framework for spatially-mapping information from diverse sources into a common reference space. Specifically, brain atlases allow annotation of gene expression, cell morphology, connectivity, and activity. In larval zebrafish, advances in genetics, imaging, and computational methods now allow the collection of such information brain-wide. However, due to technical considerations, disparate datasets may use different references and may not be aligned to the same coordinate space. Two recent larval zebrafish atlases exemplify this problem: Z-Brain, containing gene expression, neural activity and neuroanatomical segmentations, was acquired using immunohistochemical stains, while the Zebrafish Brain Browser (ZBB) was constructed from live scans of fluorescent reporters in transgenic larvae. Although different references were used, the atlases included several common transgenic patterns that provide potential 'bridges' for transforming each into the other's coordinate space. We tested multiple bridging channels and registration algorithms and found that the symmetric diffeomorphic normalization (SyN) algorithm improved live brain registration precision while better preserving cell morphology than B-spline based registrations. SyN also corrected for tissue distortion introduced during fixation. Multi-reference channel optimization provided a transformation that enabled Z-Brain and ZBB to be co-aligned with precision of approximately a single cell diameter and minimal perturbation of cell and tissue morphology. Finally, we developed software to visualize brain regions in 3-dimensions, including a virtual reality neuroanatomy explorer. This study demonstrates the feasibility of integrating whole brain datasets, despite disparate reference templates and acquisition protocols, when sufficient information is present for bridging. Increased accuracy and interoperability of zebrafish digital brain atlases will facilitate neurobiological studies.

Background

Larval stage zebrafish are an increasingly popular model for neurobiological studies. With a brain that contains an estimated 10^5 neurons, larvae are similar in complexity to adult *Drosophila*, another established neuroscience model. In both systems, researchers can deploy a wide range of genetic tools in efforts to decode patterns of neural structure and connectivity. In larval zebrafish, optical transparency and constrained physical dimensions (fitting within an imaging volume of $1000 \times 600 \times 350 \mu\text{m}$) allow the entire brain to be rapidly scanned at cellular resolution using diffraction-limited microscopy. In principle, this enables researchers to systematically analyze effects of manipulations on a brain-wide level. However, such efforts have been hampered by the absence of a comprehensive digital atlas that would provide researchers with a unified framework in which to aggregate data from different experiments and gain deeper insights from correlations between neuronal cell identity, connectivity, gene

1
2
3
4 36 expression and function within the brain. Additionally, digital atlases may more clearly delineate
5
6 37 structural boundaries that are difficult to accurately identify within individual brains, allowing for a more
7
8 38 rigorous mapping of neuroanatomical regions onto experimental data.
9

10
11 40 These longstanding problems in zebrafish neuroscience have recently been addressed by the construction
12
13 41 of digital atlases using 3-dimensional (3D) image registration techniques: the Virtual Brain Explorer for
14
15 42 Zebrafish (ViBE-Z), Z-Brain and the Zebrafish Brain Browser (ZBB) [1–3]. In these atlases, information
16
17 43 on gene expression, structure (neuronal cell bodies, glia, vasculature, ventricles, neuropil or axon tracts)
18
19 44 and measures of activity (calcium or secondary messenger activity) are consolidated within a common
20
21 45 spatial framework. By using widely-available transgenic lines or immunohistochemical stains as reference
22
23 46 templates for brain alignment, each of these atlases provides other researchers the opportunity to register
24
25 47 their own datasets into these digital spaces and take advantage of the information contained within.
26

27
28 49 ViBE-Z was the first comprehensive 3D digital brain atlas in zebrafish that used a nuclear stain for the
29
30 50 alignment of 85 high resolution scans comprising 17 immunohistochemical patterns at 2-4 days post-
31
32 51 fertilization (dpf) [3,4]. In ViBE-Z, custom algorithms were developed to correct for variations in
33
34 52 fluorescent intensity with scan depth, and a landmark approach taken to perform accurate image
35
36 53 registration and segmentation into 73 neuroanatomic regions.
37

38
39 54
40
41 55 In contrast, two more recent approaches (Z-Brain and ZBB) have generated brain atlases at 6 dpf through
42
43 56 non-linear B-spline registration using the freely available Computational Morphometry Toolkit (CMTK)
44
45 57 [5,6]. Z-Brain includes 29 immunohistochemical patterns from 899 scans which form the basis for expert
46
47 58 manual segmentation of the brain into 294 neuroanatomic regions. These partitions facilitate the analysis
48
49 59 of phospho-ERK expression for mapping neural activity [2]. In Z-Brain, each expression pattern was co-
50
51 60 scanned with tERK immunoreactivity, and registered to a single tERK-stained reference brain. For ZBB,
52
53 61 we live-imaged 354 brains from 109 transgenic lines and manually annotated the expression found in
54
55 62 each [1]. In place of tERK, a single *vglut2a:dsRed* transgenic brain was used as the reference in ZBB with
56
57 63 transgenic lines crossed and co-imaged with this channel for registration. Brain browser software enables
58
59 64 researchers to select a transgenic line labeling a selected set of neurons for monitoring and manipulating
60
61 65 circuit function.
62

63
64 66
65
66 67 While Z-Brain and ZBB are powerful datasets on their own, we saw an opportunity to merge the two
67
68 68 atlases because they are both based on confocal scans of 6 dpf larvae. This would bring to Z-Brain a large
69
70 69 number of additional transgenic lines and to ZBB, the expert manual segmentation of Z-Brain. Several
71
72

1
2
3
4 70 similarities between Z-Brain and ZBB suggested that bridging the atlases would be possible. First as
5
6 71 zebrafish rearing conditions are standardized across laboratories and fish were imaged at the same time
7
8 72 post-fertilization, Z-Brain and ZBB likely reflect the same developmental timepoint. Second, images in
9
10 73 both atlases were acquired at similar resolution (0.8 x 0.8 x 2 μm for Z-Brain; 1 x 1 x 1 or 1 x 1 x 2 μm
11 74 for ZBB) and orientation (dorsal to ventral horizontal scans). Third, despite using distinct templates
12 75 (tERK for Z-Brain and *vglut2a* for ZBB), Z-Brain and ZBB have several transgenic markers in common,
13
14 76 which provide the possibility of bridging the datasets by using these shared patterns as references for a
15
16 77 secondary registration step.
17
18 78

19 79 One of the strengths of larval zebrafish is the ability to rapidly image at cellular resolution and visualize
20 80 brain-wide neuronal morphology, providing valuable information on cell type and potential connectivity.
21 81 Z-Brain and ZBB both illustrate the feasibility of performing whole-brain registration with precision
22 82 sufficient to ensure that the 'same' neurons from different fish are aligned to within a cell diameter (~8
23 83 μm). However, a challenge for brain registration in zebrafish is to minimize local distortions, so that
24 84 cellular morphology is preserved while still allowing sufficient deformation to overcome biological
25 85 variability between individual brains or malformations due to tissue processing.
26
27
28
29
30
31 86

32
33 87 Here we describe a method to co-register ZBB and Z-Brain, bridging the two existing 6 dpf larval
34 88 zebrafish brain atlases. By using the diffeomorphic algorithm SyN in the Advanced Normalization Tools
35 89 (ANTs) software package [7,8], we were able to overcome differences in tissue shape due to fixation,
36 90 optimize the trade-off between preservation of cell morphology and global alignment, and provide precise
37 91 registration in all tested brain regions. Additionally, ANTs provided superior image registration for live-
38 92 scanned larvae, enabling us to improve the precision of registration and neuron morphology within our
39 93 original ZBB atlas, allowing us to compile a new version with increased fidelity (ZBB_{1.2}).
40
41
42
43
44 94

45 95 **Methods**

46 96 47 97 **Zebrafish lines**

48 98 In order to provide additional options for bridging ZBB and Z-Brain, we scanned two transgenic lines that
49 99 were not in the original ZBB release: *Et(gata2a:EGFP)zf81 (vmat2:GFP)* and *Tg(isl1:GFP)rw0*
50 100 (*isl1:GFP*) [9,10]. Other lines referenced in this study are *Tg(slc6a3:EGFP)ot80 (DAT:GFP)* [11], *Tg(-*
51 101 *3.2fev:EGFP)ne0214 (pet1:GFP)* [12], *y264Et* [13], *s1181tEt* [14], *Tg(gad1b:GFP)nns25 (gad1b:GFP)*
52 102 [15], *Tg(slc6a5:GFP)cf3 (glyT2:GFP)* [16], *Tg(-17.6isl2b:GFP)zc7 (isl2b:GFP)* [17], *Tg(-*
53 103 *3.4tph2:Gal4ff)y228 (tph2:Gal4)* [18], *TgBAC(slc17a6b:lox-DsRed-lox-GFP)nns14 (vglut2a:DsRed)*
54
55
56
57
58
59
60
61
62
63
64
65

1
2
3
4 104 [19], *Tg(slc17a6:EGFP)zf139* [20], *Tg(elavl3:CaMPARI(W391F+V3987L))jff9* [21],
5
6 105 *Tg(phox2b:GFP)w37* [22], *J1229aGt* [23] and several Gal4 enhancer traps from ZBB: *y304Et*, *y332Et*,
7
8 106 *y341Et*, *y351Et* and *y393Et* [1]. All *in vivo* experimental protocols were approved by the NICHD animal
9
10 107 care and use committee.

11 108

12 109 **Immunohistochemistry**

14 110 Immunolabeling was as described [2] with the following adaptations. Larvae were fixed overnight at 4°C
15
16 111 in PBS with 4% paraformaldehyde and 0.25% Triton X-100. Samples were then washed in PBS
17
18 112 containing 0.1% Triton X-100 (PBT) 3 times for 5 min. For antigen retrieval, samples were incubated in
19
20 113 150 mM Tris-HCl pH 9.0 for 5 min at room temperature (RT), followed by 15 min at 70°C and washed in
21
22 114 PBT 2 times for 5 min at RT [24]. Critically, samples were then permeabilized on ice in fresh 0.05%
23
24 115 trypsin-EDTA for no more than 5 minutes. If pigmented, samples were incubated in PBT with 1.5% H₂O₂
25
26 116 and 50 mM KOH for 15 min, rinsed 2 times in PBT and washed again for 10 min, all at RT. Samples
27
28 117 were then blocked in PBT containing 5% normal goat serum (NGS) and 0.2% bovine serum albumin
29
30 118 (BSA) for 1 hr at RT before incubation at 4°C with tERK antibodies (Cell Signaling, 4696) diluted 1:500
31
32 119 in PBT with 5% NGS and 0.2% BSA for a minimum of 6 hr. Samples were then washed with PBT 4
33
34 120 times for 30 min at RT before incubation at 4°C for a minimum of 2 hr with fluorescent secondary
35
36 121 antibodies (Alexa Fluor 488 or 548) diluted 1:1000 in PBT with 5% NGS and 0.2% BSA. Samples were
37
38 122 finally rinsed 4 times for 30 min at RT prior to imaging.

39 123

40 124 **Registration**

41 125 Registrations were performed using CMTK version 3.2.3 and ANTs version 2.1.0 running on the National
42
43 126 Institute of Health's Biowulf Linux computing cluster. Registrations were parallelized using Slurm-based
44
45 127 bash scripts available upon request. For CMTK, previously optimized registration parameters that
46
47 128 minimize computation time while maximizing precision were used (affine parameters: `registrationx --dofs`
48
49 129 `12 --min-stepsizes 1 ; elastic parameters: warpX --fast --grid-spacing 100 --smoothness-constraint-weight
50
51 130 1e-1 --grid-refine 2 --min-stepsizes 0.25 --adaptive-fix-thresh 0.25). For ANTs registrations, the
52
53 131 parameters used are cited in the relevant text and figures with optimized parameters listed in Table 1. All
54
55 132 deformable transformations are initiated with a rigid and affine step (parameters included in Table 1).
56
57 133 Aside from the use of ANTs, the basic imaging and registration workflow was performed as previously
58
59 134 described [1]. Image volumes were rendered within the Zebrafish Brain Browser (ZBB), ImageJ [25] or
60
61 135 code written in IDL (Harris Geospatial Solutions). For the conversion to/from NIFTI format required for
62
63 136 ANTs, we used the ImageJ plugin nifti_io.jar written by Guy Williams [26].`

1
2
3
4
5
6
7
8
9
10
11
12
13
14
15
16
17
18
19
20
21
22
23
24
25
26
27
28
29
30
31
32
33
34
35
36
37
38
39
40
41
42
43
44
45
46
47
48
49
50
51
52
53
54
55
56
57
58
59
60
61
62
63
64
65

138 **Volume rendering & 3D visualization**

139 Binary masks corresponding to 25 anatomical regions from Z-Brain aligned to ZBB were converted into
140 meshes using the Create Surfaces tool in the IntSeg_3D.jar plugin for ImageJ [27]. Edges for individual
141 meshes were iteratively reduced below 5000 and vertices (single-precision floating-points of the
142 triangular meshes) written as OBJ files. As there is no intrinsic color or color conventions as of yet for
143 these brain structures, we used color hue as a nominal categorical coding for each region. To maximize
144 accessibility, we rendered meshes in Extensible 3D (X3D) format, an ISO (International Organization for
145 Standardization) standard developed by the not-for-profit Web3D Consortium [28]. This format allows
146 portability between numerous tools and applications as well as deployment across a broad spectrum of
147 platforms. For the rendering, OBJs were transcoded into ImageTextureAtlas PNGs using X3D's standard
148 IndexedFaceSet to represent mesh information and then tiled at different resolutions (4096 & 8192 pixels
149 squared) using AtlasConversionScripts [29]. Additionally, dask and pyimg python libraries were used to
150 generate volume norms (image and ImageTextureAtlas files) by gradient descent. All renderings were
151 then merged into a single X3D XML scene which was losslessly compressed (in SRC/glTF) to a final size
152 of 4.5 MB. This makes the scene compact enough to be visualized on a cell phone, while retaining details
153 for visualization and editing in immersive virtual reality environments. Finally, X3D files were published
154 to HTML5 via the X3DOM library and a simple user interface created that allows for the visibility of
155 different structures to be toggled on and off. Brain meshes were converted to FBX files for import into
156 Unity using Blender 2.78a (Blender foundation, Amsterdam, NL) and mobile app development for
157 Google Cardboard VR headsets performed in Unity 5.4.2 (Unity Technologies SF, San Francisco CA)
158 using the Google VR for Unity SDK (Google, Mountain View CA). Custom scripts controlling
159 movement and mesh display were written for Unity in C#.

161 **Measurements**

162
163 *Mean Landmark Distance (MLD)*. To assess registration precision using MLDs, corresponding landmarks
164 were located and annotated on the reference brain, and on unregistered brains. In each case, landmarks
165 were chosen to be widely distributed within the brain, and readily recognized in corresponding brain
166 scans. In addition, to verify recognizability, the *vglut2a* landmarks in the reference brain were located by
167 3 blinded scorers ; mean distance from each of the 10 reference points ranged from 1.7 to 11.8 μm (mean,
168 $4.5 \pm 0.9 \mu\text{m}$). Using ImageJ, we positioned a 3 micron cube centered on each landmark in a second
169 channel for each brain scan, then, after registering the brain scan using the first channel, applied the
170 resulting transformation matrix to the second channel, using Nearest Neighbor interpolation for both

1
2
3
4 171 CMTK and ANTs. Landmark distance was taken as the distance between the geometrical center of the
5
6 172 corresponding cubes in the reference image, and in the registered image.
7
8 173 *Hausdorff distance.* We manually segmented cells in a *vglut:DsRed* brain scan in a second channel and
9 174 applied transformation matrices for registration to this second channel. Segmented cells were broadly
10
11 175 distributed to ensure that distortion measures sampled the entire brain, and cell masks conservatively
12
13 176 drawn within the boundaries of the soma. We then compared the morphology of cells after registration
14 177 (A), to their original shape (B) by calculating the partial Hausdorff distance [30]. Briefly, for every point
15
16 178 in a segmented cell mask before registration, we found the minimum distance to a point in the same mask
17
18 179 after registration. The Hausdorff distance is the maximum of all such distances, calculated for both A→B
19 180 and B→A. Because the Hausdorff distance is highly sensitive to cell alignment, and registration displaces
20
21 181 cells from their original location, we found the optimal alignment for comparisons using a two-step
22
23 182 process. First we aligned the geometric center of each cell in the original and transformed images. Second
24 183 we searched for the minimal Hausdorff distance across 4940 rigid transformations of the aligned cell,
25
26 184 within a 3 x 3 x 3 micron cube, (0.25 micron steps in each dimension). Finally, as Hausdorff distances are
27
28 185 sensitive to outliers, we used the 95th percentile distances instead of the maximum Hausdorff distance for
29
30 186 all measures [30].
31 187 *Cell volume.* For each segmented cell, we calculated its change in volume as the absolute value of the
32
33 188 fractional change in the number of pixels after application of a transformation matrix.
34 189 *Elongation index.* For each pixel in a segmented cell, we found the maximal distance (MD) to any other
35
36 190 pixel in the mask . The elongation index for a given cell was the 95th percentile largest value of MD,
37
38 191 which we take as an approximation of the diameter of the cell across its longest axis.
39 192 *Cross correlation.* Cross correlation between the tERK-stained reference brain, and registered tERK
40
41 193 stains, was performed using the `c_correlate` function within IDL version 7.0. Correlations were run
42
43 194 within eighteen 50 μm-side cube sub-regions of the image volumes that were manually selected to
44
45 195 encompass high contrast boundaries and the mean of the 18 values taken as the mean cross correlation
46 196 (MCC) for each brain in Fig. 3.
47
48 197 *Jaccard index.* Anti-tERK immunohistochemistry intensely stains tectal neuropil. Thus for measuring the
49 198 accuracy of registration of the tectal neuropil, we manually segmented the left tectal neuropil area in 6
50
51 199 confocal scans of tERK stained larvae and our reference brain. We applied transformation matrices to
52
53 200 these masks, then calculated the Jaccard index as the volume of the intersection between each registered
54
55 201 mask (A) and the reference brain (B), divided by the total volume of the union of A and B.
56 202

57 203 **Results**

205 Optimization of ANTs based registration of live *vglut2a:DsRed* image scans

206
207 Brain registration in Z-Brain and ZBB used the B-spline elastic transformation in CMTK. Before
208 attempting to co-align Z-Brain and ZBB, we tested an alternate algorithm for brain alignment, the
209 diffeomorphic symmetric normalization (SyN) method in ANTs, because: (1) SyN has been shown to
210 outperform B-spline transformations for deformable image registration in a variety of imaging modalities
211 [31,32]. (2) ANTs permits registration using multiple reference channels, potentially allowing the use of
212 multiple complementary expression patterns as references for improved registration fidelity. (3) By
213 calculating forward and reverse transformations simultaneously, SyN transformation matrices are
214 intrinsically symmetric, ensuring that bridging registrations would be unbiased and that we could easily
215 perform reciprocal transformations to register each dataset into the other's coordinate system.

216
217 To calibrate registration parameters, we assessed the alignment precision and distortion of cell
218 morphology after the registration of six representative *vglut2a:DsRed* scans to the original *vglut2a:DsRed*
219 reference brain in ZBB (*vglut2a_{ZBB}*; file *vglut-dsred-ref-01.nii.gz*, available from [33], procedure
220 summarized in Fig. 1a). Similar to CMTK we employed a three step registration within ANTs where rigid
221 and affine steps were used to initialize a deformable registration using the SyN diffeomorphic
222 transformation with cross correlation (CC) as the similarity metric. We tested a range of values for each
223 of the SyN parameters as well as the radius of the region used for cross correlation.

224
225 To measure registration precision, we visually located 10 point-based landmarks in the *vglut2a_{ZBB}* pattern
226 (Additional File 1a-c) and in each of the 6 *vglut2a:DsRed* confocal scans. We then used the *vglut:DsRed*
227 channel for registration, and applied the resulting transformation matrix to the landmarks in each of the 6
228 brains. We measured the distance of each landmark from its location in the *vglut2a_{ZBB}* reference brain
229 (Additional File 1a,d). We designated the average of the 10 distances the 'Mean Landmark Distance'
230 (MLD). To assess the amount of distortion in cell shapes produced by the parameter sets, we segmented
231 107 cells in an unregistered *vglut2a:DsRed* confocal scan (Additional File 2), and applied each
232 transformation matrix to this set of cell masks. Changes in cell shape were measured using the partial
233 Hausdorff distance for each cell after registration compared to its original shape (see Methods).

234
235 Next we plotted the MLD against the Hausdorff distance and located points along the Pareto frontier (Fig.
236 1b) of these two measures. These points represent potentially optimal transformations, where registration
237 accuracy can only be improved by increasing distortion, or vice versa. To distinguish between these
238 points, we examined two additional measures of distortion: the change in cell volume (Fig. 1c) and

1
2
3
4 239 maximal elongation (Fig. 1d). Three transformations showed statistically significantly reduced distortion
5 compared to CMTK for both measures, and we selected the one (Fig. 1b, point d) with the greatest
6 240 precision for further testing. With this set of parameters (see Table 1, **live registration**), mean registration
7 241 error was within the diameter of a single neuron for both ANTs and CMTK (MLD for ANTs 6.7 ± 0.3
8 242 μm , for CMTK $7.6 \pm 0.4 \mu\text{m}$; N = 6 brains, paired t-test $p=0.056$). However, cell morphology was better
9 243 preserved using ANTs (Hausdorff Distance for ANTs 2.30 ± 0.14 , CMTK 2.37 ± 0.14 ; N = 107 cells,
10 244 paired t-test $p=0.013$), especially within ventral structures such as the hypothalamus and the caudal
11 245 medulla oblongata (Fig. 1e).
12
13
14
15
16 246

17 247
18
19 248 We next examined whether these registration parameters also improved precision for the co-aligned
20 transgenic lines. For ZBB, we co-scanned transgene and enhancer trap expression patterns with the
21 249 *vglut2a:dsRed* transgene, allowing us to register each expression pattern to *vglut2a*_{ZBB}. We first compared
22 250 the overlap and morphology of the Mauthner cells from brain scans of three different individuals of
23 251 transgenic line *J1229aGt* [23]. Overlap of Mauthner cell bodies was similar for CMTK and ANTs (Fig.
24 252 1f,g). However, in CMTK registered images, the Mauthner axon was distorted in the caudal medulla,
25 253 whereas axon morphology was preserved with ANTs. Second, in our previous work, we assessed the
26 254 precision of CMTK registration using line *y339Et* by independently scanning two sets of three larvae,
27 255 producing an average for each set, and visually comparing the result. With CMTK we had noted
28 256 misalignment of approximately 1 cell diameter in the neuropil of the optic tectum (Fig. 1h). This was
29 257 substantially improved with ANTs, where there was much closer alignment of the two averages (Fig. 1i).
30
31
32
33
34
35
36 258
37
38 259

39 260 **Improved precision of ZBB after registration using ANTs**

40 261
41
42 262 We next recompiled ZBB using ANTs to register the entire set of 354 brain scans from 109 different
43 263 transgenic lines that were part of ZBB, then as before, averaged multiple larvae to create a representation
44 264 of each transgenic line, masked the average stacks to remove expression outside the brain and re-imported
45 265 the resulting images into our Brain Browser software. We refer to this new recompilation of the atlas as
46 266 ZBB_{1.2}. Unprocessed and registered brain images are available online [35].
47
48
49
50
51 267

52 268 To determine whether ZBB_{1.2} was a quantitative improvement over ZBB, we identified two
53 269 conspicuously labeled cells or landmarks in each of 12 transgenic lines from the atlas (Additional File 3).
54 270 We marked these positions in each of the three brain scans for each line, then, after registration,
55 271 calculated the distance between corresponding points in each pair of brains. The mean of these distances
56 272 measures how precisely landmarks are registered across the three brains. We performed this procedure
57
58
59
60
61
62
63
64
65

1
2
3
4 273 first for brains registered using CMTK, then for the same set of brains registered using ANTs, allowing us
5
6 274 to compare MLDs for the two methods (Fig. 2a-b). Overall, landmark distances decreased from ZBB to
7
8 275 ZBB_{1,2} ($10.8 \pm 1.02 \mu\text{m}$ to $8.1 \pm 0.83 \mu\text{m}$; N = 24 landmarks, paired t-test p=0.008), indicating that
9
10 276 ZBB_{1,2} has significantly improved precision, and confirming that the new atlas is accurate to
11
12 277 approximately the diameter of a single neuron. The improvement was greatest deeper in the brain (Fig. 2c
13
14 278 ; linear regression, N=24, p=0.003) with the largest improvement for the caudal hypothalamus in line
15
16 279 y341, where increased alignment precision was associated with noticeably reduced distortion between the
17
18 280 three brain scans (Fig. 2d).

19 281
20 282 Additionally, we inspected regions of ZBB_{1,2} where we had noticed poor registration precision or
21
22 283 pronounced cell distortion in the original ZBB. One such area was the dorsal thalamus, where cell
23
24 284 morphology was noticeably perturbed after elastic registration with CMTK, with cell somas stretching
25
26 285 across the midline (Fig. 2e). In ZBB_{1,2} cells retained a rounded morphology with distinct cell clusters on
27
28 286 the left and right sides of the brain (Fig. 2f). Similarly, distortions in cell shape that were apparent in the
29
30 287 caudal hypothalamus in ZBB, were absent in ZBB_{1,2} (Fig. 2g,h). In the caudolateral medulla, we
31
32 288 previously obtained poor registration, with expression extending to regions outside the neural tube (Fig.
33
34 289 2i). In ZBB_{1,2}, patterns had improved bilateral symmetry and were correctly confined to the neural tube
35
36 290 (Fig. 2j). Finally, we noticed that the posterior commissure was poorly aligned between larvae leading to
37
38 291 a defasciculated appearance in ZBB (Fig. 2k), whereas this tract had the expected tightly bundled
39
40 292 appearance in ZBB_{1,2} (Fig. 2l). Together, these observations confirm that ZBB_{1,2} is a more faithful
41
42 293 representation of the transgenic lines. Not only is cell morphology better preserved, but global registration
43
44 294 precision is improved compared to the original ZBB atlas.

45 295 46 296 **Optimization of ANTs registration parameters for fixed tissue**

47 297
48 298 The Z-Brain atlas was derived by registering brain scans to a single brain that was fixed, permeabilized
49
50 299 and immunostained for tERK expression. We therefore anticipated that tERK would be a useful channel
51
52 300 for bridging the two atlases, if we could first successfully register a tERK stained *vglut2a:DsRed*
53
54 301 expressing brain to ZBB_{1,2}. Therefore, we fixed and stained a transgenic *vglut2a:DsRed* larva for tERK,
55
56 302 and registered the tERK pattern to ZBB_{1,2} using the *vglut2a* pattern. We used the resulting image as our
57
58 303 ZBB tERK reference brain (tERK_{ZBB} ; file *terk-ref-02.nii.gz* available from [33]).

59 304
60 305 In addition to the tERK reference brain, Z-Brain contains an average tERK representation from 197 tERK
61
62 306 stained larvae, which we thought might serve as a bridge between atlases. During studies on pERK-based

1
2
3
4 307 activity mapping, we had previously generated a dataset of 167 tERK stained brains and therefore used
5
6 308 these to create our own average tERK representation by registering them to tERK_{ZBB}. However, during
7
8 309 this process, we noticed a high degree of variability between tERK stained brains, most salient in poor
9
10 310 labeling of ventral brain structures and in deformation of the optic tectum neuropil.
11
12 311 Immunohistochemistry for tERK proved highly sensitive to staining parameters with the trypsin activity,
13
14 312 permeabilization duration, and antigen retrieval having the strongest effects. Variability in fixed tissue
15
16 313 was most apparent in the optic tectum, where high trypsin activity tended to disrupt morphology and
17
18 314 reduce the volume of the tectal neuropil (Fig. 3b,c). These local distortions were not resolved by
19
20 315 deformable image registration: alignment to tERK_{ZBB} with the same parameters optimized for live *vglut2a*
21
22 316 based registration failed to correct the reduced tectal neuropil volume (Fig. 3d,e ; asterisk) and often
23
24 317 created an artifact where the neuropil zone failed to abut the underlying cellular layer labeled by *vglut2a*
25
26 318 expression (Fig. 3d,e ; arrowheads).

27
28 319
29 320 We therefore varied the registration parameters that were optimal for live *vglut2a* registration, to find
30
31 321 settings that best rectified the variable tissue morphology following fixation and permeabilization
32
33 322 (process summarized in Fig. 3a). For optimization of fixed tissue registration, we used a set of 6 tERK
34
35 323 stained brains (including the Z-Brain tERK reference), iteratively varied parameters for registration to
36
37 324 tERK_{ZBB} and assessed registration fidelity. For measuring precision, we were not able to identify
38
39 325 unambiguous landmarks within the optic tectum, so we instead calculated the cross-correlation between
40
41 326 each of the aligned tERK stains and tERK_{ZBB} within small volumes, including parts of the tectum (Fig.
42
43 327 3f,g). To verify that the 'fixed brain' parameters that yielded the greatest cross correlation did in fact
44
45 328 improve registration within the tectum, we manually segmented the tectal neuropil in the same 6 brains,
46
47 329 applied the transformation matrix to each mask, and calculated the Jaccard index for overlap with the
48
49 330 segmented neuropil in tERK_{ZBB}. Parameters for fixed brain registration produced a significant increase in
50
51 331 overlap, compared to the live brain parameters (Fig. 3h,i) and visual inspection confirmed that the
52
53 332 morphology of the optic tectum neuropil after registration was greatly improved (Fig. 3j,k). We therefore
54
55 333 used ANTs with the fixed brain parameters (Table 1, **fixed registration**) to register our 167 tERK stained
56
57 334 brains to tERK_{ZBB}, and generated an average tERK representation comparable to the 197 tERK average in
58
59 335 Z-Brain (Fig. 3l,m).

336 337 **Inter-atlas registration using multi-channel diffeomorphic transformation**

338
339 Z-Brain and ZBB incorporated eight expression patterns that we judged sufficiently similar to act either
340
as templates for bridging the datasets and/or to provide metrics for assessing the precision of a bridging

1
2
3
4 341 registration (Table 2, Additional File 4). For example, *vglut2a*_{ZBB} is a confocal scan of DsRed in a single
5
6 342 larva from transgenic line *TgBAC(slc17a6b:loxP-DsRed-loxP-GFP)nns14*, whereas Z-Brain includes
7
8 343 *Tg(slc17a6:EGFP)zf139*. In both cases, reporter expression is regulated by the same bacterial artificial
9
10 344 chromosome [15,20]. Crossing these two lines allowed us to scan DsRed and EGFP in the same larva and
11
12 345 confirm that the patterns were largely congruous, potentially allowing us to use *vglut2a* expression to
13
14 346 bridge the two atlases. Likewise, the expression patterns of *tERK*, *elavl3*, *isl2b*, *vmat2* in Z-Brain and
15
16 347 ZBB appeared sufficiently similar to provide templates for atlas co-registration.

17
18 349 Taking advantage of the ability of ANTs to use of multiple reference channels concurrently, we compared
19
20 350 the effect of combinatorial use of complementary reference channels for inter-atlas registration (process
21
22 351 summarized in Fig. 4a). We used seven expression patterns to evaluate registration precision: *vglut2a*,
23
24 352 *isl2b*, *vmat2*, tERK, *isl1*, *gad1b* and *glyT2*. For each pattern we identified a set of 4-10 point-based
25
26 353 landmarks that could be identified in corresponding ZBB and Z-Brain images and that were widely
27
28 354 distributed to represent diverse brain regions (total of 41 landmarks ; Additional File 5). We marked these
29
30 355 points in each set of images, registered Z-Brain images to ZBB_{1,2} images, measured the distance between
31
32 356 cognate landmarks and calculated the mean landmark distance for each of the seven expression patterns.
33
34 357 We used two summary measures of registration precision. The first metric (M₁) was the mean of MLDs
35
36 358 for the three patterns that were not used to drive registration (*isl1*, *gad1b* and *glyT2*). Although these
37
38 359 channels measure precision independent of the patterns for atlas registration, they are relatively sparse
39
40 360 and do not assess precision across the whole brain. Thus, to provide a global measure of precision, we
41
42 361 also used a second metric (M₂) that was the mean of all seven MLDs: those in M₁ plus four of the patterns
43
44 362 used as references for registration — *vglut2a*, tERK, *isl2b* and *vmat2*.

45
46 364 Using CMTK, minimal M₁ and M₂ scores were obtained using the average *vmat2* pattern as the reference
47
48 365 (Fig. 4b; mean MLD for 41 landmarks $14.9 \pm 1.3 \mu\text{m}$). We therefore registered all images in Z-Brain to
49
50 366 ZBB using the *vmat2* average in each dataset as the reference channel. We observed severe tissue
51
52 367 distortions in several brain regions, with noticeable flattening of the torus longitudinalis as well as gross
53
54 368 tissue distortions, particularly in ventral brain regions (Fig. 4c,d; ZBrain-CMTK). Next we used the
55
56 369 ANTs SyN algorithm to register the atlases. Ideally, patterns for registration should include information
57
58 370 throughout the brain. Because ANTs can use multiple concurrent reference channels to derive an optimal
59
60 371 transformation matrix, we speculated that the best possible transformation would be achieved by a
61
62 372 combination of channels with complementary information. We therefore produced an inter-atlas
63
64 373 transformation matrix for every combination of the *elavl3*, *isl2b*, *vglut2a*_{AV} (*vglut2a* average brain),
65
66 374 *vmat2*, tERK_{ZBB} (tERK single brain) and tERK_{AV} (tERK average brain) patterns as references. Because Z-

1
2
3
4 375 Brain used fixed samples, we used the registration parameters optimized for the greater variability present
5
6 376 in fixed tissue. Multi-channel registration significantly reduced M_1 and M_2 values compared to any single
7
8 377 channel alone and to transformations obtained using CMTK. The registration obtained with *vglut2a*,
9 378 *tERK_{ZBB}*, *vmat2* and *isl2b* gave the lowest global metric (M_2) value and an M_1 score within 10% of the
10 379 lowest scoring combination (Fig. 4b). With these parameters, the MLD was $9.1 \pm 0.8 \mu\text{m}$ (N=41
11 380 landmarks) and the overt tissue distortions noted after elastic registration were far less salient (Fig. 4c,d;
12
13 381 ZBrain-SyN). We therefore applied the transformation matrix obtained with this set of channels to the
14
15 382 database of gene expression patterns in Z-Brain to align them to $ZBB_{1,2}$, and used the inverse of the
16
17 383 transformation generated by SyN to register $ZBB_{1,2}$ to the Z-Brain coordinate system. We imported all Z-
18
19 384 Brain expression patterns not previously represented in the database into $ZBB_{1,2}$, producing a total of 133
20
21 385 expression patterns.

22 386
23
24 387 The accuracy of the inter-atlas registration is evident when comparing the location of cells that are present
25
26 388 in both datasets, such as those labeled by *pet1:GFP*. The Z-Brain transformed pattern closely matches the
27
28 389 transgene expression pattern in $ZBB_{1,2}$ within the superior raphe (Fig. 4e — note however that
29
30 390 unexpectedly, the line in $ZBB_{1,2}$ also labels a set of more rostral cells not apparent in Z-Brain). Both
31
32 391 atlases also include lines labeling the Mauthner cells. After registration, Mauthner cells in the atlases
33
34 392 substantially overlapped, although they were several microns more medially positioned in $ZBB_{1,2}$ (Fig.
35
36 393 4f). Expression in the *DAT:GFP* line in $ZBB_{1,2}$ overlapped well with the tyrosine hydroxylase stain from
37
38 394 Z-Brain in the pretectum (Fig. 4g), although again, the $ZBB_{1,2}$ pattern was slightly more medial than in Z-
39
40 395 Brain. Caudally, the *glyT2:GFP* transgenic line labels glycinergic neurons in longitudinal columns in the
41
42 396 medulla oblongata [36]. These columns were closely aligned after $ZBB_{1,2}$ was registered to Z-Brain (Fig.
43
44 397 4h).

45 398
46 399 Although best practice is to align directly to either ZBB or Z-Brain, because many researchers will have
47
48 400 already registered data sets to either ZBB or Z-Brain, or for cases where it may not be possible to directly
49
50 401 register a dataset, we have provided transformation matrixes and detailed instructions to quickly re-align
51
52 402 datasets to either of the coordinate systems ([37] ; Additional File 6).

53 403 54 404 **Neuroanatomical visualization**

55 405
56 406 Z-Brain includes 294 masks that represent anatomically defined brain regions or discrete clusters of cells
57
58 407 present in transgenic lines. We selected 113 of these masks that delineate neuroanatomical regions and
59
60 408 transformed them into the $ZBB_{1,2}$ coordinate system. We had previously defined a small number of our

1
2
3
4 409 own anatomical masks by thresholding clusters of neuronal cell bodies located in well-defined brain
5
6 410 regions. However the Z-Brain masks are more comprehensive, have smoother boundaries and include
7
8 411 both the cell bodies and neuropil for a given region (Fig. 4i-1). We therefore imported the Z-Brain masks
9
10 412 into ZBB_{1,2}, replacing most of our existing masks. We also modified the Brain Browser software to
11
12 413 automatically report the neuroanatomical identity of a selected pixel, or to display the boundaries of the
13
14 414 region encompassing a selected point. The updated software and rebuilt database in ZBB_{1,2} can be
15
16 415 downloaded from our website [38].

17
18 417 Finally, as the Zebrafish Brain Browser's strength is primarily in two dimensions (i.e., the visualization of
19
20 418 horizontal, transverse, and sagittal slices through the brain), we decided to develop interactive tools to
21
22 419 better facilitate 3D exploration. The use of 3D graphics to represent complex structure can also provide a
23
24 420 more intuitive sensory experience that avoids cognitive bias or misinterpretation inadvertently introduced
25
26 421 by two dimensional reductions [39,40]. By taking advantage of stereoscopy and vestibular-enhanced
27
28 422 parallax (head tracking), the more immersive and holistic experience of Virtual Reality (VR) can also
29
30 423 significantly improve performance of basic tasks like searching and making comparisons [41,42]. We
31
32 424 therefore implemented our Zebrafish Brain Browser in both an open Web3D platform (X3D) and a
33
34 425 custom game engine (Unity). First, we converted masks representing anatomical regions to meshes and
35
36 426 built a Web3D interface using X3D to inspect the spatial relationship between different brain regions
37
38 427 (Fig. 5a,b), available online [43]. Users can navigate within the brain using any web browser, rotating and
39
40 428 zooming into brain regions to better interrogate larval neuroanatomy. Second, using the Unity platform
41
42 429 we wrote a VR app to view the brain and neuroanatomical regions. By running the app on a cell phone,
43
44 430 and inserting it into an inexpensive Google cardboard viewer, users can 'walk into' the brain, and see from
45
46 431 the inside the inter-relationship between neuroanatomical domains (Fig. 5c,d), available for download
47
48 432 [44].

49 433

46 434 **Discussion**

49 435
50 436 Digitized data-derived brain atlases provide an opportunity to continuously integrate new information and
51
52 437 iteratively improve data accuracy within a common spatial framework. Thus, as methods evolve and
53
54 438 technology improves, new insights can be easily added to existing data to provide an increasingly rich
55
56 439 view of brain structure and function. Because the entire larval zebrafish brain can be rapidly imaged at
57
58 440 cellular resolution, it is possible to envisage an atlas that combines detailed information on cell type
59
60 441 (including gene expression and morphology), connectivity and activity under a variety of different
61
62 442 physiological conditions. At present, biological variability presents an obstacle, as brain regions contain

1
2
3
4
5
6
7
8
9
10
11
12
13
14
15
16
17
18
19
20
21
22
23
24
25
26
27
28
29
30
31
32
33
34
35
36
37
38
39
40
41
42
43
44
45
46
47
48
49
50
51
52
53
54
55
56
57
58
59
60
61
62
63
64
65

443 multiple intermingled cell types that are not positioned in precisely the same manner between larvae. To
444 compensate for this in the existing zebrafish brain atlases, multiple individuals of a given line are sampled
445 and averaged to generate a representative expression pattern. Current atlases are thus essentially heat
446 maps of gene expression or activity. Despite this spatial ambiguity, aggregating information from
447 different sources into the same spatial framework still provides valuable indicators of cell type, gene co-
448 expression, and neural activity under defined conditions.

449
450 Ideally different atlas projects might use the same reference brain, however in practice the choice of a
451 reference is often dictated by study-specific experimental requirements. For example, despite the
452 deformations introduced by fixation and permeabilization, a fixed brain is essential for activity mapping
453 using pERK immunohistochemistry. In contrast, we were able to take advantage of the optical
454 transparency of larvae to rapidly scan and register several hundred individuals representing more than 100
455 different transgenic lines. For our purposes, the *TgBAC(slc17a6b:loxP-DsRed-loxP-GFP)nns14* line was
456 ideal, because through Cre injection, we generated a *vglut2a:GFP* line with an almost identical pattern,
457 allowing us to co-register lines with either GFP or RFP fluorescence. However, we have also used pan-
458 neuronal Cerulean or mCardinal as a reference channel when green and red channels both contain useful
459 information on transgene expression. Our work now demonstrates that it is feasible to contribute to
460 community efforts at building an integrated map of brain structure, expression and activity, while
461 allowing reference image selection to be guided by technical considerations.

462
463 One caveat to this conclusion is that deformable image registration can easily introduce artifacts into cell
464 morphology if parameters are not carefully monitored and constrained. Indeed, a special challenge for
465 brain registration in zebrafish is preserving the local morphology of neuronal cell bodies and axons, while
466 permitting sufficient deformation to correct for biological differences and changes in brain structure
467 arising from tissue fixation and permeabilization. Thus, while B-spline registration with CMTK produced
468 acceptable inter-atlas alignment, it also introduced noticeable distortions into local brain structure that
469 affected neuronal cell morphology. Such artifacts were particularly severe in ventral brain regions such as
470 the caudal hypothalamus, and may therefore be due to differences in ventral signal intensity between the
471 datasets. In ZBB, in order to compensate for the increase in light diffraction with tissue depth, we
472 systematically increased laser intensity with confocal scan progression (z-compensation). As a result, the
473 Z-Brain and ZBB datasets are comparable in dorsal brain regions, but there is a noticeable discrepancy
474 ventrally which may account for the loss of registration fidelity. Alternatively, although z-compensation
475 partially corrects for reduced fluorescent intensity, there is a noticeable drop-off in image resolution in
476 ventral regions; the resulting loss of information may lead to lower quality registration. Registration

1
2
3
4 477 algorithms that allow parameters to vary by depth may ameliorate the effects of these physical imaging
5
6 478 constraints.

7 479
8
9 480 Nevertheless, the symmetrical diffeomorphic transformation in ANTs provides a solution to these
10
11 481 problems. For live tissue, we found parameters that allowed the ANTs SyN transform to achieve similar
12
13 482 or better registration precision than previously achieved using CMTK, while significantly reducing
14
15 483 distortions in tissue structure and neuronal cell morphology. In our hands, permeabilization of fixed tissue
16
17 484 tended to produce variable changes in neuropil structure which was most salient in the optic tectum.
18
19 485 Specifically, neuropil volume was diminished when fresh aliquots of trypsin were used for extended
20
21 486 durations. These artifacts can be minimized by stringent oversight of reagent viridity. However, by
22
23 487 calibrating SyN parameters to permit larger deformations, we were able to accommodate the variability
24
25 488 introduced in tissue processing.

26 490 Currently, limitations of the SyN registration algorithm in ANTs are the large memory demands (73 GB
27
28 491 for a single channel registration) and long computational times (3-5 hours for a single channel using 24
29
30 492 cores) required for registration of images with a resolution sufficient for the brain-wide visualization of
31
32 493 neuronal morphology (e.g., 1000 x 600 x 350 pixels). For multi-channel registrations, memory demands
33
34 494 and computation time were even greater: 106 GB for 6 channels taking over 16 hours on 24 cores.
35
36 495 However, our present ANTs SyN parameters likely can be further optimized to reduce these demands. For
37
38 496 instance, our parameters currently include 10 iterations of transformation matrix optimization at full
39
40 497 image resolution. From our experience, these full resolution registration cycles do not significantly
41
42 498 increase precision, but greatly increase computation time. Thus, computation time may be reduced by
43
44 499 adjusting registration resolution as well as other parameters without adversely affecting registration
45
46 500 quality. Although computational resources did not present a bottleneck for registering a small number of
47
48 501 samples, this increase in the demands of a single registration made it difficult to optimize registration
49
50 502 parameters as extensively as we had done previously with CMTK [1]. By reducing computation time, we
51
52 503 would be able to explore more comprehensively the parameter space available with SyN and evaluate
53
54 504 alternative diffeomorphic transforms available with ANTs that may provide still better registration
55
56 505 fidelity.

57 506
58
59 507 An obstacle to systematically calibrating registration parameters is finding a suitable metric to
60
61 508 quantitatively evaluate precision. This is a recognized problem, and it is not clear that a general solution
62
63 509 exists [34]. Here, we primarily assessed precision by measuring the distance between visually-located
64
65 510 landmarks in the reference brain, and registered images. However, this method has two drawbacks: (1) it

1
2
3
4 511 relies on the accuracy with which these landmarks are located, and (2) at least for our sample set, a
5
6 512 relatively limited set of landmarks could reliably be identified. We obtained similar results when we
7
8 513 assessed precision using cross-correlation within localized image neighborhoods that included high
9
10 514 contrast internal image boundaries (data not shown). In registering live *vglut2a:DsRed* image stacks, we
11
12 515 noted the trade-off between accurate global brain alignment and biologically plausible cell morphology.
13
14 516 Thus we also used a set of measures to assess changes in the morphology of manually segmented cells
15
16 517 (Hausdorff distance, elongation index and cell volume). Finally, we also inspected the output of every
17
18 518 transformation to subjectively judge registration quality.

19 519
20 520 This study demonstrates that the ANTs diffeomorphic symmetric normalization algorithm (SyN)
21 521 advances upon elastic registration for precise registration of whole brain images in larval zebrafish and is
22
23 522 markedly better at preserving neuronal cell morphology. By systematically testing SyN registration
24
25 523 parameters for registering images acquired using live scans, we improved the ZBB atlas. Then, after
26
27 524 calibrating registration parameters for fixed tissue and using multi-channel optimization, we were able to
28
29 525 align the Z-Brain atlas into the ZBB coordinate space, and vice-versa, achieving co-registration accuracy
30
31 526 to approximately the diameter of a single neuron. We believe that integrating the information present in
32
33 527 each of these atlases produces a richer framework for future studies of structural and functional
34
35 528 relationships within the nervous system. Large digital datasets such as those present in brain atlases can
36
37 529 be used for many types of bioinformatic analysis. Z-Brain and ZBB already include software that can be
38
39 530 used to explore the larval zebrafish brain, and we hope that integrating these datasets into a single
40
41 531 coordinate system, will help to stimulate the development of additional computational tools and methods
42
43 532 for querying this information.

44 533

45 534 **Availability of supporting data**

46 535
47 536 All individual brain scans, both before and after registration to a ZBB reference brain, are available in the
48
49 537 *GigaScience* repository, GigaDB [35]. The GigaDB repository also includes the set of reference brains
50
51 538 used for ZBB [33] and the transformation matrices used to convert between ZBB and Z-Brain coordinate
52
53 539 systems [37].

54 540

55 541 **Abbreviations**

- 56 542
- 57 543 ac, anterior commissure
- 58 544 Ce, cerebellum
- 59 545 DT, Thalamus
- 60 546 GT, Griseum tectale

1
2
3
4 547 Ha, Habenula
5 548 Hc, Hypothalamus caudal zone
6 549 Hi, Hypothalamus intermediate zone
7
8 550 MO, Medulla oblongata
9 551 NXm, Vagus motor neurons
10 552 OB, Olfactory bulb
11 553 OE, Olfactory epithelium
12 554 ON, Olfactory nerve
13 555 IO, Inferior olive
14 556 LC, Locus coeruleus
15 557 MN, Mauthner neuron
16 558 MO, Medulla oblongata
17 559 Pal, Pallium
18 560 pc, posterior commissure
19 561 Po, preoptic region
20 562 Pr, Pretectum
21 563 SR, Superior raphe
22 564 Teg, Tegmentum
23 565 TeOn, Optic tectum neuropil
24 566 TG, Trigeminal ganglion
25 567 TL, Torus longitudinalis
26 568 TS, Torus semicircularis
27
28
29

30 570
31

32 571 **Competing Interests**

33
34 572

35 573 The authors declare that they have no competing interests.
36

37 574
38

39 575 **Authors' Contribution**

40 576

41
42 577 GDM and HAB conceived the experiments. GDM, KMT, EJH and HAB optimized ANTS for zebrafish
43
44 578 brain registration. GDM, MB and AKG contributed confocal brain scans and generated meshes. NFP
45
46 579 developed the X3D/HTML5 based browser. DDN developed the Unity VR browser. GDM and HAB
47 580 wrote the manuscript. All authors approved the final manuscript.
48

49 581

50 582 **Acknowledgements**

51 583
52
53

54 584 This work was supported by the Intramural Research Program of the *Eunice Kennedy Shriver* National
55 585 Institute for Child Health and Human Development (NICHD) and utilized the high-performance
56
57 586 computational capabilities of the Biowulf Linux cluster at the National Institutes of Health, Bethesda, MD
58
59 587 [45]. We thank Owen Randlett for valuable discussion and help checking the correspondence of *vglut2a*

1
2
3
4
5
6
7
8
9
10
11
12
13
14
15
16
17
18
19
20
21
22
23
24
25
26
27
28
29
30
31
32
33
34
35
36
37
38
39
40
41
42
43
44
45
46
47
48
49
50
51
52
53
54
55
56
57
58
59
60
61
62
63
64
65

588 expression patterns. We are grateful to Sinisa Pajevic (NIH/CIT) for advice on computational procedures
589 and to M. Okan Irfanglu and Neda Sadeghi (NICHD) for guidance in optimizing ANTs parameters.

590
591 **References**

592
593 1. Marquart GD, Tabor KM, Brown M, *et al.* A 3D Searchable Database of Transgenic Zebrafish Gal4
594 and Cre Lines for Functional Neuroanatomy Studies. *Front Neural Circuits* 2015; **9**:78.
595
596 2. Randlett O, Wee CL, Naumann EA, *et al.* Whole-brain activity mapping onto a zebrafish brain atlas.
597 *Nat Methods* 2015; **12**:1039–1046.
598
599 3. Ronneberger O, Liu K, Rath M, *et al.* ViBE-Z: a framework for 3D virtual colocalization analysis in
600 zebrafish larval brains. *Nat Methods* 2012; **9**:735–42.
601
602 4. Rath M, Nitschke R, Filippi A, Ronneberger O, Driever W. Generation of high quality multi-view
603 confocal 3D datasets of zebrafish larval brains suitable for analysis using Virtual Brain Explorer (ViBE-
604 Z) software. *Protoc Exch* 2012.
605
606 5. Portugues R, Feierstein CE, Engert F, Orger MB. Whole-Brain Activity Maps Reveal Stereotyped,
607 Distributed Networks for Visuomotor Behavior. *Neuron* 2014; **81**:1328–1343.
608
609 6. Rohlfing T, Maurer CR Jr. Nonrigid image registration in shared-memory multiprocessor environments
610 with application to brains, breasts, and bees. *IEEE Trans Inf Technol Biomed* 2003; **7**:16–25.
611
612 7. Avants BB, Epstein CL, Grossman M, Gee JC. Symmetric diffeomorphic image registration with
613 cross-correlation: Evaluating automated labeling of elderly and neurodegenerative brain. *Med Image Anal*
614 2008; **12**:26–41.
615
616 8. Avants BB, Tustison NJ, Song G, Cook PA, Klein A, Gee JC. A reproducible evaluation of ANTs
617 similarity metric performance in brain image registration. *NeuroImage* 2011; **54**:2033–2044.
618
619 9. Higashijima S, Hotta Y, Okamoto H. Visualization of cranial motor neurons in live transgenic
620 zebrafish expressing green fluorescent protein under the control of the islet-1 promoter/enhancer. *J*
621 *Neurosci* 2000; **20**:206–18.
622
623 10. Wen L, Wei W, Gu W, *et al.* Visualization of monoaminergic neurons and neurotoxicity of MPTP in
624 live transgenic zebrafish. *Dev Biol* 2008; **314**:84–92.
625
626 11. Xi Y, Yu M, Godoy R, Hatch G, Poitras L, Ekker M. Transgenic zebrafish expressing green
627 fluorescent protein in dopaminergic neurons of the ventral diencephalon. *Dev Dyn* 2011; **240**:2539–47.
628
629 12. Lillesaar C, Stigloher C, Tannhauser B, Wullimann MF, Bally-Cuif L. Axonal projections originating
630 from raphe serotonergic neurons in the developing and adult zebrafish, *Danio rerio*, using transgenics to
631 visualize raphe-specific pet1 expression. *J Comp Neurol* 2009; **512**:158–82.
632
633 13. Tabor KM, Bergeron SA, Horstick EJ, *et al.* Direct activation of the Mauthner cell by electric field
634 pulses drives ultra-rapid escape responses. *J Neurophysiol* 2014; **112**:834–844.

- 1
2
3
4 623 14. Scott EK, Baier H. The cellular architecture of the larval zebrafish tectum, as revealed by gal4
5 624 enhancer trap lines. *Front Neural Circuits* 2009; **3**:13.
6
7 625 15. Satou C, Kimura Y, Hirata H, Suster ML, Kawakami K, Higashijima S. Transgenic tools to
8 626 characterize neuronal properties of discrete populations of zebrafish neurons. *Development* 2013;
9 627 **140**:3927–31.
10
11
12 628 16. McLean DL, Fan J, Higashijima S, Hale ME, Fetcho JR. A topographic map of recruitment in spinal
13 629 cord. *Nature* 2007; **446**:71–5.
14
15 630 17. Pittman AJ, Law MY, Chien CB. Pathfinding in a large vertebrate axon tract: isotypic interactions
16 631 guide retinotectal axons at multiple choice points. *Development* 2008; **135**:2865–71.
17
18 632 18. Yokogawa T, Hannan MC, Burgess HA. The dorsal raphe modulates sensory responsiveness during
19 633 arousal in zebrafish. *J Neurosci* 2012; **32**:15205–15215.
20
21
22 634 19. Satou C, Kimura Y, Higashijima S. Generation of multiple classes of V0 neurons in zebrafish spinal
23 635 cord: progenitor heterogeneity and temporal control of neuronal diversity. *J Neurosci* 2012; **32**:1771–83.
24
25 636 20. Bae YK, Kani S, Shimizu T, *et al.* Anatomy of zebrafish cerebellum and screen for mutations
26 637 affecting its development. *Dev Biol* 2009; **330**:406–26.
27
28 638 21. Fosque BF, Sun Y, Dana H, *et al.* Labeling of active neural circuits in vivo with designed calcium
29 639 integrators. *Science* 2015; **347**:755–760.
30
31
32 640 22. Nechiporuk A, Linbo T, Poss KD, Raible DW. Specification of epibranchial placodes in zebrafish.
33 641 *Development* 2007; **134**:611–623.
34
35 642 23. Burgess HA, Johnson SL, Granato M. Unidirectional startle responses and disrupted left-right co-
36 643 ordination of motor behaviors in robo3 mutant zebrafish. *Genes Brain Behav* 2009; **8**:500–11.
37
38 644 24. Inoue D, Wittbrodt J. One for All—A Highly Efficient and Versatile Method for Fluorescent
39 645 Immunostaining in Fish Embryos. *PLOS ONE* 2011; **6**:e19713.
40
41 646 25. Schneider CA, Rasband WS, Eliceiri KW. NIH Image to ImageJ: 25 years of image analysis. *Nat*
42 647 *Methods* 2012; **9**:671–675.
43
44
45 648 26. Williams G. *NIfTi Input/Output*. <https://imagej.nih.gov/ij/plugins/nifti.html> (last accessed, 22 March
46 649 2017)
47
48 650 27. Heisenberg M, Schmid B. *IntSeg 3D*. http://3dviewer.neurofly.de/IntSeg_3D (last accessed, 22 March
49 651 2017)
50
51 652 28. Web3D Consortium. *Open Standards for Real-Time 3D Communication*. <http://www.web3d.org/> (last
52 653 accessed, 22 March 2017)
53
54
55 654 29. Vicomtech-IK4. *AtlasConversionScripts*. <https://github.com/VolumeRC/AtlasConversionScripts> (last
56 655 accessed, 22 March 2017)
57
58 656 30. Huttenlocher DP, Klanderman GA, Rucklidge WJ. Comparing images using the Hausdorff distance.
59 657 *IEEE Trans Pattern Anal Mach Intell* 1993; **15**:850–863.
60
61
62
63
64
65

1
2
3
4 658 31. Klein A, Andersson J, Ardekani BA, *et al.* Evaluation of 14 nonlinear deformation algorithms applied
5 659 to human brain MRI registration. *NeuroImage* 2009; **46**:786–802.
6
7 660 32. Murphy K, Ginneken B van, Reinhardt JM, *et al.* Evaluation of Registration Methods on Thoracic
8 661 CT: The EMPIRE10 Challenge. *IEEE Trans Med Imaging* 2011; **30**:1901–1920.
9
10 662 33. *ZBB Reference Brains*.http://helix.nih.gov/~BurgessLab/reference_brains.zip (last accessed, 22 March
11 663 2017) To be replaced with GigaDB DOI upon publication
12
13
14 664 34. Rohlfing T. Image Similarity and Tissue Overlaps as Surrogates for Image Registration Accuracy:
15 665 Widely Used but Unreliable. *IEEE Trans Med Imaging* 2012; **31**:153–163.
16
17 666 35. *ZBB Raw and Registered Brain Images* GigaDB DOI to be provided upon publication
18
19 667 36. Kinkhabwala A, Riley M, Koyama M, *et al.* A structural and functional ground plan for neurons in the
20 668 hindbrain of zebrafish. *Proc Natl Acad Sci U A* 2011; **108**:1164–9.
21
22 669 37. *ZBB-ZBrain Transformation Matrices*. <https://helix.nih.gov/~BurgessLab/zb主-zbrain.zip> (last
23 670 accessed, 22 March 2017) To be replaced with GigaDB DOI upon publication
24
25 671 38. *Zebrafish Brain Browser*.<https://science.nichd.nih.gov/confluence/display/burgess/Brain+Browser>
26 672 (last accessed, 22 March 2017)
27
28 673 39. Ota D, Loftin B, Saito T, Lea R, Keller J. Virtual reality in surgical education. *Comput Biol Med*
29 674 1995; **25**:127–137.
30
31 675 40. Ware C, Franck G. Viewing a graph in a virtual reality display is three times as good as a 2D diagram.
32 In: *Proceedings of 1994 IEEE Symposium on Visual Languages.*; 1994:182–183.
33
34 676 41. Bowman DA, McMahan RP. Virtual Reality: How Much Immersion Is Enough? *Computer* 2007;
35 677 **40**:36–43.
36
37 678 42. Henry JAG, Polys NF. The effects of immersion and navigation on the acquisition of spatial
38 knowledge of abstract data networks. *Procedia Comput Sci* 2010; **1**:1737–1746.
39
40 679 43. *Zebrafish Anatomy Explorer*.
41 <http://metagrid2.sv.vt.edu/~npolys/NIH/Burgess/ZebraFishBrowser/ZebrafishBrowser.html> (last
42 680 accessed, 22 March 2017)
43
44 681 44. *Virtual reality brain browser*.
45 <https://science.nichd.nih.gov/confluence/display/burgess/Brain+Browser#BrainBrowser-vrfishbrain> (last
46 682 accessed, 22 March 2017)
47
48 683 45. *High Performance Computing at the NIH. 2016*. <https://hpc.nih.gov> (last accessed, 22 March 2017)
49
50 684
51 685
52 686
53 687
54 688
55 689 **Figure legends**
56
57 690
58
59 691 **Table 1. ANTs command parameters for image registration**
60
61
62
63
64
65

1
2
3
4 692
5
6 693 **Table 2. Brain images in ZBB and Z-Brain that were used as templates for registration and/or for**
7 **measurement of registration precision.**
8

9 695
10
11 696
12 697 **Figure 1. Optimization of parameters for registration of live brain scans using ANTs**

14 698 (a) Overview of parameter optimization for live brain scans using ANTs. A calibration set of 6
15 *vglut2a:DsRed* confocal stacks with 10 point-based landmarks and 107 cell masks were registered to the
16 699 *vglut2a_{ZBB}* reference with the same 10 point-based landmarks defined (left). MLDs for landmarks and
17 700 Hausdorff distance for transformed cell masks compared to their originals were measured for each
18 701 parameter set (middle). Optimal parameters selected from these metrics (b-d) were used to re-register all
19 702 lines generating ZBB_{1,2} where MLD was measured from 2 additional landmarks in each of 12 co-aligned
20 703 patterns (right).
21 704

22 705 (b) Hausdorff distance for cell shape comparison plotted against MLD for 68 sets of parameters tested
23 706 using ANTs (grey and blue circles) and after registration using CMTK (orange). Blue circles labeled a-f
24 707 indicate the Pareto frontier.
25

26 708 (c) Mean absolute change in cell volume (as a fraction of the original volume) produced by
27 709 transformations resulting from parameter sets a-f and CMTK in (b). * $p < 0.05$, compared to CMTK.
28

29 710 (d) Mean elongation index for cells after registration using parameter sets a-f and CMTK in (b). Dashed
30 711 line shows index for cells before registration — all transformations produced a significant increase in
31 712 compared to the untransformed cells. * $p < 0.05$, compared to CMTK. (e) Horizontal section through the
32 713 medulla oblongata in *vglut2a_{ZBB}*, and of a representative *vglut2a:DsRed* brain after registration using
33 714 CMTK or ANTs. Distortion artifacts are indicated (arrow). Scale bar 50 μm
34

35 715 (f,g) Horizontal section in *J1229aGt* showing expression of GFP in the Mauthner cell and axon
36 716 (arrowheads) for three individual larvae (pseudo-colored red, green and blue). Registration was performed
37 717 with CMTK (f) or ANTs (g). Scale bar 100 μm .
38

39 718 (h,i) Transverse section through the optic tectum in two separate average brain images (colored green and
40 719 magenta) for *y393Et*. For each brain image, we independently scanned three individual brains and
41 720 registered them using CMTK (h) or ANTs (i). Scale bar 100 μm .
42

43 721
44 722 **Figure 2. Improved precision of transgene representations in ZBB_{1,2}**

45 723 (a) Mean landmark distances for 24 landmarks, after registration with CMTK and ANTs. Dotted line
46 724 indicates 1:1 ratio.
47

48 725 (b) Boxplot of data in (a). * paired t-test, N=12 lines, $p = 0.019$
49
50
51
52
53

1
2
3
4 726 (e) Difference in MLD between ANTs and CMTK plotted against distance from the dorsal-most point in
5
6 727 the brain.
7
8 728 (d) Horizontal section through the caudal hypothalamus of three individual *y341Et* larvae as well as their
9 729 pseudo-colored superimposition following registration with CMTK (top row) or ANTs (bottom row).
10
11 730 (e,f) Horizontal section through the thalamus showing the averaged representation of enhancer trap line
12
13 731 *y304Et*, where individual brains were registered with CMTK for ZBB (e), or with ANTs for ZBB_{1,2} (f).
14 732 Arrow indicates neurons that are artificially elongated across the midline. Scale bar 100 μm.
15
16 733 (g,h) Transverse section through the caudal hypothalamus showing the average enhancer trap line *y269Et*
17 734 brain registered with CMTK (g) or with ANTs (h). Arrow shows distortion of cells causing the caudal
18
19 735 hypothalamus to appear dorsally elongated. Scale bar 50 μm.
20
21 736 (i,j) Transverse section through the medulla oblongata showing the average *phox2b:GFP* brain with
22
23 737 CMTK (i) or ANTs (j). Scale bar 50 μm.
24
25 738 (k,l) Horizontal projection through the posterior commissure (arrow) for the average *y351Et* brain
26 739 obtained with CMTK (k) or ANTs (l). Scale bar 100 μm.
27
28 740

29 741 **Figure 3. Optimization of ANTs registration parameters for fixed tissue**
30

31 742 (a) Overview of parameter optimization for fixed brain scans using ANTs. A calibration set of 6 tERK
32
33 743 confocal stacks with segmentations of the tectal neuropil were registered to tERK_{ZBB}, a tERK and
34 744 *vglut2a:DsRed* confocal scan previously aligned to the *vglut2a*_{ZBB} reference (left). MCCs were calculated
35
36 745 between eighteen 50 μm-side cube high-contrast sub-regions in the calibration set and in the tERK_{ZBB}
37
38 746 reference to identify parameters that maximized MCC (f,g) and improved the Jaccard index of tectal
39 747 neuropil segmentation (h) while compensating for fixation artifacts (c,e,k) (middle). These optimized
40
41 748 ANTs parameters allow for the accurate registration of fixed tissue and the generation of a tERK average
42
43 749 reference (tERK_{AV}) useful for bridging live and fixed tissue registrations (right).
44
45 750 (b,c) Horizontal section through the optic tectum of tERK immunostained(red) *vglut2a:DsRed* (green)
46 751 larvae, using diluted (b, sample A) or fresh trypsin (c, sample B). Asterisk indicates missing area of
47
48 752 tectal neuropil due to permeabilization artifact.
49
50 753 (d,e) Horizontal section through the same stacks as in (b,c) registered to tERK_{ZBB} using the parameters
51 754 previously optimized for live registration. Gray shows the ZBB_{1,2} *vglut2a:DsRed* pattern. Arrowheads
52
53 755 highlight regions where tERK in the optic tectum neuropil fails to closely abut the adjacent glutamatergic
54
55 756 cellular layer.
56
57 757 (f) MCC for tERK expression after registration of 6 brains to tERK_{ZBB}, varying each of the parameters for
58 758 the ANTs SyN transform, starting with the parameters that gave the best registration for live
59
60
61
62
63
64
65

1
2
3
4 759 *vglut2a:DsRed* based registration (SyN[0.05,6,0.5]). Bottom right: MCCs after varying the radius of the
5
6 760 cross-correlation metric used during registration.
7
8 761 (g) MCCs for tERK in the same brains as in (f), after combining the two best parameter sets from (f)
9 762 (SyN[0.1,6,0.5] and SyN[0.05,6,0]) to assess further improvement in registration precision. Yellow box
10 763 highlights the final optimal parameter set.
11
12 764 (h) Jaccard index for overlap of the manually segmented tectal neuropil of the reference brain, with each
13 765 of the 6 brains in the calibration set. $p < 0.01$
14
15 766 (i) 3D view of overlap between segmented tectal neuropils from tERK_{ZBB} (red) and the Z-Brain tERK
16 767 reference brain (green), after registration with ANTs using parameter optimal for live registration, fixed
17 768 registration and CMTK.
18
19 769 (j,k) Same brains as in (d,e), but after registration to tERK_{ZBB} using the parameters optimized for fixed
20 770 tissue registration.
21
22 771 (l,m) Horizontal section through the optic tectum showing tERK expression (red) and *vglut2a:DsRed*
23 772 expression (green) in ZBB_{1,2} (l) and Z-Brain (m). Matching slices within the optic tectum were selected;
24 773 because the rotation around the y-axis is slightly different, sections are different within the medulla.
25
26 774
27
28
29
30
31
32
33

34 777 **Figure 4. Transformation between Z-Brain and ZBB coordinate systems using multi-channel**
35
36 778 **registration**

37 779 (a) Overview of bridging Z-Brain and ZBB using ANTs multi-channel registration. Combinations of 5
38 780 patterns common between Z-Brain and ZBB (*vglut2a_{AV}*, tERK_{ZBB}, *vmat2*, *isl2b* and *elavl3*) were used
39 781 guide multi-channel bridging registrations (left). MLDs for 41 landmarks in *gad1b*, *glyT2*, *isl1*, *isl2b*,
40 782 tERK, *vglut2a*, and *vmat2* expression were measured for all reference channel combinations (middle).
41 783 The combination of *vglut2a_{AV}*, tERK_{ZBB}, *vmat2*, and *isl2b* enabled the most accurate bridging of ZBB and
42 784 Z-Brain allowing the combination of the large collection of live transgenic lines of ZBB with the fixed
43 785 tissue techniques and expert neuroanatomic segmentations of Z-Brain (right).
44 786 (b) MLDs for the expression patterns of *gad1b*, *glyT2*, *isl1*, *isl2b*, tERK_{ZBB}, *vglut2a* and *vmat2* and M₁
45 787 and M₂ metrics after registration of Z-Brain to ZBB_{1,2} using either CMTK or ANTs SyN with fixed-tissue
46 788 registration parameters and the indicated combination of reference channels (*vglut2a*, tERK_{ZBB}, *vmat2*,
47 789 *isl2b*, and *elavl3*). Note, similar results were obtained using tERK_{AV} instead of the tERK_{ZBB}, but are
48 790 omitted for clarity. The combination of reference channels selected for co-registration of Z-Brain and
49 791 ZBB is highlighted.
50
51
52
53
54
55
56
57
58
59
60
61
62
63
64
65

1
2
3
4 792 (c) Transverse section through the caudal optic tectum showing the *vglut2a* pattern in ZBB_{1,2}, Z-Brain, Z-
5 793 Brain after registration to ZBB with CMTK (Z-Brain-CMTK), or with ANTs (Z-Brain-SyN). The torus
6 794 longitudinalis (TL) is well separated from tectal neurons in live scans, but less so in fixed tissue (arrows).
7
8 795 The TL appears flattened after CMTK registration, but retains normal morphology after registration with
9
10 796 ANTs SyN.
11
12 797 (d) Transverse sections as in (c), but slightly more caudal with contrast increased to highlight ventral
13 798 distortion artifacts produced by registration (arrowheads).
14
15 799 (e-h) Brain Browser views in the ZBB_{1,2} coordinate (e,f) or Z-Brain coordinate (g,h) space. Scale bars 25
16 800 μm except 50 μm in (e)
17
18 801 (e) Horizontal (top) and sagittal (bottom) sections, comparing the *pet1:GFP* expression pattern in the
19 802 superior raphe in ZBB_{1,2} (red) and Z-Brain after transformation to the ZBB coordinate system (green).
20
21 803 (f) Horizontal (top) and transverse (bottom) sections through the medulla oblongata, showing the
22 804 expression of *y264Et* from ZBB_{1,2} (red) and *s1181Et* from Z-Brain after transformation to ZBB_{1,2} (green),
23 805 which both label the Mauthner cells (arrowhead).
24
25 806 (g) Horizontal (top) and transverse (bottom) sections through the pretectum, comparing the expression of
26 807 *DAT:GFP* from ZBB_{1,2} after transformation to Z-Brain (red) and anti-tyrosine hydroxylase staining in Z-
27 808 Brain (green).
28
29 809 (h) Horizontal (top) and transverse (bottom) sections through the medulla oblongata for *glyT2:GFP* from
30 810 ZBB_{1,2} after transformation to Z-Brain (red) and the same transgenic line in Z-Brain (green).
31
32 811 (i-l) Brain Browser horizontal sections showing manually segmented regions transformed from the Z-
33 812 Brain coordinate system to ZBB_{1,2} (white outlines) compared to regions previously defined in ZBB
34 813 obtained by thresholding expression patterns in transgenic lines (magenta). Regions are the torus
35 814 longitudinalis (i), habenula (j), anterior commissure (k) and trigeminal ganglion (l).
36
37
38
39
40
41
42
43
44

816 **Figure 5. 3D visualization of brain browser data**

45 817 (a) X3D zebrafish brain shown in HTML5 Web browser and (b) Virginia Tech HyperCube (CAVE)
46 818 (c) Virtual reality brain rendered using the Unity Game Engine for stereoscopic viewing using the Google
47 819 Cardboard viewer. (d) In the VR browser, brain regions are selected using a menu on the floor of the
48 820 virtual arena.
49
50
51
52

53 821

54 822 **Additional Material**

55 823

56 824 **Additional File 1.pdf**

57 825 **Point-based landmarks for quantification of live-scan registration precision.**
58
59
60
61
62
63
64
65

1
2
3
4 826 (a) Landmarks used for measuring registration precision. Position specifies the coordinates on *vglut2a_{ZBB}*
5
6 827 (transverse, sagittal, horizontal planes). View indicates whether the image plane shown in (b) is or
7
8 828 transverse (T), horizontal (H), or sagittal (S). MLDs represent the average precision for each landmark for
9 829 the set of 6 calibration brains, after registration with CMTK or ANTs.
10
11 830 (b) Images of the landmarks in *vglut2a_{ZBB}* (red) used for measuring precision superimposed on *elavl3*
12
13 831 (gray).
14 832 (c) Position of the landmarks superimposed on horizontal (top) and sagittal (bottom) maximum
15
16 833 projections of *elavl3* through the brain.
17
18 834 (d) Horizontal maximum projections showing the landmark point (red dot), and the position of the
19 835 corresponding landmarks in the six calibration brains after registration (green dots) superimposed on
20
21 836 *vglut2a_{ZBB}*. Scale bar 20 μ m.

22
23 837
24 838

26 839 **Additional File 2.pdf**

27 840 **Cells segmented for assessing distortion introduced by registration**

29 841 (a) Position of manually segmented cells for measurement of distortion introduced by registration. Views
30
31 842 show the same cells (individually color coded) superimposed on horizontal (top) and sagittal (bottom)
32
33 843 maximum *elavl3* brain projections.
34 844 (b) Two examples of cells showing (left to right): original confocal image, segmentation mask, mask after
35
36 845 alignment with CMTK, and mask after alignment with ANTs.

37 846

39 847 **Additional File 3.pdf**

41 848 **Point-based landmarks labeled by transgenic lines**

42 849 (a) Transgenic line landmarks used for measuring registration precision of the zebrafish brain browser
43
44 850 atlas. Coordinates give the transverse, horizontal, sagittal position. Letter in square brackets designates
45
46 851 Right side [R], Left side [L], or Midline [M]. The mean and standard error of the landmark distances for
47
48 852 the three brains per landmark are indicated for CMTK and ANTs.

49 853 (b) Position of the landmarks superimposed on horizontal (top) and sagittal (bottom) maximum *elavl3*
50
51 854 brain projections.

52 855

54 856 **Additional File 4.pdf**

56 857 **ZBB and Z-Brain expression patterns used for atlas registration**

57 858 Brain Browser 3D projections of corresponding expression patterns in Z-Brain (left) and ZBB (right) used
58
59 859 for calibrating and verifying the precision of inter-atlas registration. The top 5 patterns were

1
2
3
4
5
6
7
8
9
10
11
12
13
14
15
16
17
18
19
20
21
22
23
24
25
26
27
28
29
30
31
32
33
34
35
36
37
38
39
40
41
42
43
44
45
46
47
48
49
50
51
52
53
54
55
56
57
58
59
60
61
62
63
64
65

860 combinatorially used to drive registration, while the bottom 3 were used for assessing precision. Middle
861 images show Z-Brain patterns after registration to ZBB.

862
863 **Additional File 5.pdf**

864 **Point-based landmarks for measuring precision of Z-Brain/ZBB co-registration**

865 (a) Transgenic line and tERK-stain landmarks used for measuring registration precision of registration
866 between Z-Brain and ZBB. Coordinates are in transverse, horizontal, sagittal sections. Letters in square
867 brackets designates Right side [R], Left side [L], or Midline [M]. Color blocks correspond to points in (b).
868 (b) Position of the landmarks superimposed on horizontal (top) and sagittal (bottom) maximum brain
869 projections.

870
871 **Additional File 6.doc**

872 **Instructions for using transformation matrices to convert between ZBB and Z-Brain coordinate**
873 **systems.**

1
2
3
4
5
6
7
8
9
10 **High precision registration between zebrafish brain atlases**
11 **using symmetric diffeomorphic normalization**
12
13
14
15
16
17
18
19
20
21

22 Gregory D. Marquart^{1,2}, Kathryn M. Tabor¹, Eric J. Horstick¹, Mary Brown¹,
23 Alexandra K. Geoca¹, Nicholas F. Polys³, Damian Dalle Nogare¹ and Harold A. Burgess^{1*}
24
25
26
27
28
29
30
31
32
33
34
35
36

37 ¹ Division of Developmental Biology, *Eunice Kennedy Shriver* National Institute of Child Health
38 and Human Development, Bethesda, MD 20892

39 ² Neuroscience and Cognitive Science Program, University of Maryland, College Park, MD
40 20742

41 ³ Advanced Research Computing, Department of Computer Science, Virginia Polytechnic
42 Institute and State University, Blacksburg, VA 24061

43
44
45
46
47
48
49 * Contact: burgessha@mail.nih.gov ; 301-402-6018
50
51
52
53

54 Running title: High fidelity inter-atlas registration using ANTs SyN transform

55 Keywords: zebrafish, atlas, ANTs, SyN, registration, diffeomorphism, normalization, brain
56 imaging, transgenic, virtual reality, Unity, X3D
57
58
59
60
61

1
2
3
4 **Abstract**
5
6

7
8 Atlases provide a framework for information from diverse sources to be spatially mapped and integrated
9 into a common reference space. In particular, brain atlases allow regional annotation of gene expression,
10 cell morphology, connectivity and activity. In larval zebrafish, advances in genetics, imaging and
11 computational methods have enabled the collection of large datasets providing such information on a
12 whole brain scale. However, datasets from different sources may not be aligned to the same spatial
13 coordinate system, because technical considerations may necessitate use of different reference templates.
14 Two recent brain atlases for larval zebrafish exemplify this problem. The Z-Brain atlas contains
15 information on gene expression, neural activity and neuroanatomical segmentation acquired using
16 immunohistochemical staining of fixed tissue. In contrast, the Zebrafish Brain Browser (ZBB) atlas was
17 constructed from live scans of fluorescent reporter genes in transgenic larvae. Although different
18 reference brains were used, the two atlases included several transgene patterns in common that provide
19 potential 'bridges' for transforming each into the other's coordinate space. We tested multiple bridging
20 channels and registration algorithms. The symmetric diffeomorphic normalization (SyN) algorithm in
21 ANTs improved the precision of live brain registration while better preserving cell morphology than the
22 previously used B-spline elastic registration algorithm. SyN could also be calibrated to correct for tissue
23 distortion introduced during fixation and permeabilization. Multi-reference channel optimization provided
24 a transformation that enabled Z-Brain and ZBB to be co-aligned with high precision and minimal
25 perturbation of cell and tissue morphology. Finally, we developed software to visualize brain regions in 3-
26 dimensions, including a virtual reality neuroanatomy explorer. This study demonstrates the feasibility of
27 integrating whole brain datasets, despite disparate reference templates and acquisition protocols, when
28 sufficient information is present for bridging. This increased accuracy and interoperability of digital brain
29 atlases in larval zebrafish will facilitate future neurobiological studies.

30 Atlases provide a framework for spatially-mapping information from diverse sources into a common
31 reference space. Specifically, brain atlases allow annotation of gene expression, cell morphology,
32 connectivity, and activity. In larval zebrafish, advances in genetics, imaging, and computational methods
33 now allow the collection of such information brain-wide. However, due to technical considerations,
34 disparate datasets may use different references and may not be aligned to the same coordinate space. Two
35 recent larval zebrafish atlases exemplify this problem: Z-Brain, containing gene expression, neural
36 activity and neuroanatomical segmentations, was acquired using immunohistochemical stains, while the
37 Zebrafish Brain Browser (ZBB) was constructed from live scans of fluorescent reporters in transgenic
38 larvae. Although different references were used, the atlases included several common transgenic patterns
39 that provide potential 'bridges' for transforming each into the other's coordinate space. We tested multiple

1
2
3
4 35 [bridging channels and registration algorithms and found that the symmetric diffeomorphic normalization](#)
5 [\(SyN\) algorithm improved live brain registration precision while better preserving cell morphology than](#)
6 36 [B-spline based registrations. SyN also corrected for tissue distortion introduced during fixation. Multi-](#)
7 37 [reference channel optimization provided a transformation that enabled Z-Brain and ZBB to be co-aligned](#)
8 [with precision of approximately a single cell diameter and minimal perturbation of cell and tissue](#)
9 38 [morphology. Finally, we developed software to visualize brain regions in 3-dimensions, including a](#)
10 39 [virtual reality neuroanatomy explorer. This study demonstrates the feasibility of integrating whole brain](#)
11 [datasets, despite disparate reference templates and acquisition protocols, when sufficient information is](#)
12 40 [present for bridging. Increased accuracy and interoperability of zebrafish digital brain atlases will](#)
13 41 [facilitate neurobiological studies.](#)
14
15
16
17
18
19
20
21
22

23 46 **Background**

24 47
25 48
26 49 Larval stage zebrafish are an increasingly popular model for neurobiological studies. With a brain that
27 50 contains an estimated 10^5 neurons, larvae are similar in complexity to adult *Drosophila*, another
28 51 established neuroscience model. In both systems, researchers can deploy a wide range of genetic tools in
29 52 efforts to decode patterns of neural structure and connectivity. In larval zebrafish, optical transparency
30 53 and constrained physical dimensions (fitting within an imaging volume of $1000 \times 600 \times 350 \mu\text{m}$) allow
31 54 the entire brain to be rapidly scanned at cellular resolution using diffraction-limited microscopy. In
32 55 principle, this enables researchers to systematically analyze effects of manipulations on a brain-wide
33 56 level. However, such efforts have been hampered by the absence of a comprehensive digital atlas that
34 57 would provide researchers with a unified framework in which to aggregate data from different
35 58 experiments and gain deeper insights from correlations between neuronal cell identity, connectivity, gene
36 59 expression and function within the brain. Additionally, digital atlases may more clearly delineate
37 60 structural boundaries that are difficult to accurately identify within individual brains, allowing for a more
38 61 rigorous mapping of neuroanatomical regions onto experimental data.
39
40
41
42
43
44
45
46
47
48
49

50 63 These longstanding problems in zebrafish neuroscience have recently been addressed by the construction
51 64 of digital atlases using ~~three~~3-dimensional (3D) image registration techniques: the Virtual Brain Explorer
52 65 for Zebrafish (ViBE-Z), Z-Brain and the Zebrafish Brain Browser (ZBB) [1–3]. In these atlases,
53 66 information on gene expression, structure (neuronal cell bodies, glia, vasculature, ventricles, neuropil or
54 67 axon tracts) and measures of activity (calcium or secondary messenger activity) are consolidated within a
55 68 common spatial framework. By using widely-available transgenic lines or immunohistochemical stains as
56 69 reference templates for brain alignment, each of these atlases provides other researchers the opportunity
57
58
59
60
61
62
63
64
65

1
2
3
4 70 to register their own datasets into these digital spaces and take advantage of the information contained
5
6 71 within.

7 72
8
9 73 ViBE-Z was the first comprehensive ~~three-dimensional~~3D digital brain atlas in zebrafish that used a
10 74 nuclear stain for the alignment of 85 high resolution scans comprising 17 immunohistochemical patterns
11 75 at 2-4 days post-fertilization (dpf) [3,4]. In ViBE-Z, custom algorithms were developed to correct for
12 76 variations in fluorescent intensity with scan depth, and a landmark approach taken to perform accurate
13 77 image registration and segmentation into 73 neuroanatomic regions.
14
15
16
17
18 78

19 79 In contrast, two more recent approaches (Z-Brain and ZBB) have generated brain atlases at 6 dpf through
20 80 non-linear B-spline registration using the freely available Computational Morphometry Toolkit (CMTK)
21 81 [5,6]. Z-Brain includes 29 immunohistochemical patterns from 899 scans which form the basis for expert
22 82 manual segmentation of the brain into 294 neuroanatomic regions. These partitions facilitate the analysis
23 83 of phospho-ERK expression for mapping neural activity [2]. In Z-Brain, each expression pattern was co-
24 84 scanned with tERK immunoreactivity, and registered to a single tERK-stained reference brain. For ZBB,
25 85 we live-imaged 354 brains from 109 transgenic lines and manually annotated the expression found in
26 86 each [1]. In place of tERK, a single *vglut2a:dsRed* transgenic brain was used as the reference in ZBB with
27 87 transgenic lines crossed and co-imaged with this channel for registration. Brain browser software enables
28 88 researchers to select a transgenic line labeling a selected set of neurons for monitoring and manipulating
29 89 circuit function.
30
31
32
33
34
35
36
37
38 90

39 91 While Z-Brain and ZBB are powerful datasets on their own, we saw an opportunity to merge the two
40 92 atlases because they are both based on confocal scans of 6 dpf larvae. This would bring to Z-Brain a large
41 93 number of additional transgenic lines and to ZBB, the expert manual segmentation of Z-Brain. Several
42 94 similarities between Z-Brain and ZBB suggested that bridging the atlases would be possible. First as
43 95 zebrafish rearing conditions are standardized across laboratories and fish were imaged at the same time
44 96 post-fertilization, Z-Brain and ZBB likely reflect the same developmental timepoint. Second, images in
45 97 both atlases were acquired at similar resolution (0.8 x 0.8 x 2 μ m for Z-Brain; 1 x 1 x 1 or 1 x 1 x 2 μ m
46 98 for ZBB) and orientation (dorsal to ventral horizontal scans). Third, despite using distinct templates
47 99 (tERK for Z-Brain and *vglut2a* for ZBB), Z-Brain and ZBB have several transgenic markers in common,
48 100 which provide the possibility of bridging the datasets by using these shared patterns as references for a
49 101 secondary registration step.
50
51
52
53
54
55
56
57
58 102
59
60
61
62
63
64
65

1
2
3
4 103 One of the strengths of larval zebrafish is the ability to rapidly image at cellular resolution and visualize
5
6 104 brain-wide neuronal morphology, providing valuable information on cell type and potential connectivity.
7
8 105 Z-Brain and ZBB both illustrate the feasibility of performing whole-brain registration with precision
9
10 106 sufficient to ensure that the 'same' neurons from different fish are aligned to within a cell diameter (~10-8
11 107 μm). However, a challenge for brain registration in zebrafish is to minimize local distortions, so that
12
13 108 cellular morphology is preserved while still allowing sufficient deformation to overcome biological
14 109 variability between individual brains or malformations due to tissue processing.
15

16 110
17 111 Here we describe a method to co-register ZBB and Z-Brain, bridging the two existing 6 dpf larval
18 112 zebrafish brain atlases. By using the diffeomorphic algorithm SyN in the Advanced Normalization Tools
19 113 (ANTs) software package [7,8], we were able to overcome differences in tissue shape due to fixation,
20 114 optimize the trade-off between preservation of cell morphology and global alignment, and provide precise
21 115 registration in all tested brain regions. Additionally, ANTs provided superior image registration for live-
22 116 scanned larvae, enabling us to improve the precision of registration and neuron morphology within our
23 117 original ZBB atlas, allowing us to compile a new version with increased fidelity (ZBB_{1.2}).
24
25
26
27
28
29

30 118

31 119 **Methods**

32 120

33 121 **Zebrafish lines**

34 122 In order to provide additional options for bridging ZBB and Z-Brain, we scanned two transgenic lines that
35 123 were not in the original ZBB release: *Et(gata2a:EGFP)zf81 (vmat2:GFP)* and *Tg(isl1:GFP)rw0*
36 124 (*isl1:GFP*) [9,10]. ~~Aside from the use of ANTs, the basic imaging and registration workflow was~~
37 125 ~~performed as previously described [1].~~ Other lines referenced in this study are *Tg(slc6a3:EGFP)ot80*
38 126 (*DAT:GFP*) [11], *Tg(-3.2fev:EGFP)ne0214 (Pp2et1:GFP)* [12], *y264Et* [13], *s1181tEt* [14],
39 127 *Tg(gad1b:GFP)nns25 (gad1b:GFP)* [15], *Tg(slc6a5:GFP)cf3 (glyT2:GFP)* [16], *Tg(-17.6isl2b:GFP)zc7*
40 128 (*isl2b:GFP*) [17], *Tg(-3.4tph2:Gal4ff)y228 (tph2:Gal4)* [18], *TgBAC(slc17a6b:lox-DsRed-lox-*
41 129 *GFP)nns14 (vglut2a:dsRedDsRed)* [19], *Tg(slc17a6:EGFP)zf139* [20],
42 130 *Tg(elavl3:CaMPARI(W391F+V3987L))jf9* [21], *Tg(phox2b:GFP)w37* [22], *J1229aGt* [23] and several
43 131 Gal4 enhancer traps from ZBB: *y304Et*, *y332Et*, *y341Et*, *y351Et* and *y393Et* [1]. All *in vivo* experimental
44 132 protocols were approved by the NICHD animal care and use committee.
45
46
47
48
49
50

51 133

52 134 **Immunohistochemistry**

53 135 Immunolabeling was as described [2] with the following adaptations. Larvae were fixed overnight at 4°C
54 136 in PBS with 4% paraformaldehyde and 0.25% Triton X-100. Samples were then washed in PBS
55
56
57
58
59
60
61
62
63
64
65

1
2
3
4 137 containing 0.1% Triton X-100 (PBT) 3 times for 5 min. For antigen retrieval, samples were incubated in
5
6 138 150 mM Tris-HCl pH 9.0 for 5 min [at room temperature \(RT\)](#), followed by 15 min at 70°C and washed in
7
8 139 PBT 2 times for 5 min [at RT](#) [24]. Critically, samples were then permeabilized on ice in fresh 0.05%
9
10 140 trypsin-EDTA for no more than 5 minutes. If pigmented, samples were incubated in PBT with 1.5% H₂O₂
11
12 141 and 50 mM KOH for 15 min, rinsed 2 times in PBT and washed again for 10 min, [all at RT](#). Samples
13
14 142 were then blocked in PBT containing 5% normal goat serum (NGS) and 0.2% bovine serum albumin
15
16 143 (BSA) for 1 hr [at RT](#) before incubation at 4°C with tERK antibodies (Cell Signaling, 4696) diluted 1:500
17
18 144 in PBT with 5% NGS and 0.2% BSA for a minimum of 6 hr. Samples were then washed with PBT 4
19
20 145 times for 30 min [at RT](#) before incubation at 4°C for a minimum of 2 hr with fluorescent secondary
21
22 146 antibodies (Alexa Fluor 488 or 548) diluted 1:1000 in PBT with 5% NGS and 0.2% BSA. Samples were
23
24 147 finally rinsed 4 times for 30 min [at RT](#) prior to imaging.

148 149 **Registration-**

150 Registrations were performed using CMTK version 3.2.3 and ANTs version 2.1.0 running on the National
151 Institute of Health’s Biowulf Linux computing cluster. Registrations were parallelized using Slurm-based
152 bash scripts available upon request. For CMTK, previously optimized registration parameters that
153 minimize computation time while maximizing precision were used ([affine parameters: registrationx --dofs](#)
154 [12 --min-stepsize 1 ; elastic parameters: ~~and~~ warpx --fast --grid-spacing 100 --smoothness-constraint-](#)
155 [weight 1e-1 --grid-refine 2 --min-stepsize 0.25 --adaptive-fix-thresh 0.25](#)). For ANTs registrations, the
156 parameters used are cited in the relevant text and figures with optimized parameters listed in Table 1. [All](#)
157 [deformable transformations are initiated with a rigid and affine step \(parameters included in Table 1\).](#)
158 [Aside from the use of ANTs, the basic imaging and registration workflow was performed as previously](#)
159 [described \[1\].](#) Image volumes were rendered within the Zebrafish Brain Browser (ZBB), ImageJ [25] or
160 code written in IDL (Harris Geospatial Solutions). For the conversion to/from NIfTI format required for
161 ANTs, we used the ImageJ plugin nifti_io.jar written by Guy Williams [26].

162 163 **Volume rendering & 3D visualization-**

164 Binary masks corresponding to 25 anatomical regions from Z-Brain aligned to ZBB were converted into
165 meshes using the Create Surfaces tool in the IntSeg_3D.jar plugin for ImageJ [27]. Edges for individual
166 meshes were iteratively reduced below 5000 and vertices (single-precision floating-points of the
167 triangular meshes) written as OBJ files. As there is no intrinsic color or color conventions as of yet for
168 these brain structures, we used color hue as a nominal categorical coding for each region. To maximize
169 accessibility, we rendered meshes in Extensible 3D (X3D) format, an ISO (International Organization for
170 Standardization) standard developed by the not-for-profit Web3D Consortium [28]. This format allows

1
2
3
4 171 portability between numerous tools and applications as well as deployment across a broad spectrum of
5
6 172 platforms. For the rendering, ~~previously generated~~ OBJs were transcoded into ImageTextureAtlas PNGs
7
8 173 ~~used using~~ X3D's standard IndexedFaceSet to represent mesh information and then tiled at different
9
10 174 resolutions (4096 & 8192 pixels squared) using AtlasConversionScripts [29]. Additionally, dask and
11
12 175 pyimg python libraries were used to generate volume norms (image and ImageTextureAtlas files) by
13
14 176 gradient descent. All renderings were then merged into a single X3D XML scene which was losslessly
15
16 177 compressed (in SRC/gITF) to a final size of 4.5 MB. This makes the scene compact enough to be
17
18 178 visualized on a cell phone, ~~yet still while~~ retaining details for visualization and editing in ~~more~~-immersive
19
20 179 virtual reality environments. Finally, X3D files were published to HTML5 via the X3DOM library and a
21
22 180 simple user interface created that allows for the visibility of different structures to be toggled on and off.
23
24 181 Brain meshes were converted to FBX files for import into Unity using Blender 2.78a (Blender foundation,
25
26 182 Amsterdam, NL) and mobile app development for Google Cardboard VR headsets performed in Unity
27
28 183 5.4.2 (Unity Technologies SF, San Francisco CA) using the Google VR for Unity SDK (Google,
29
30 184 Mountain View CA). Custom scripts controlling movement and mesh display were written for Unity in
31
32 185 C#.

31 187 Measurements Statistics.

32
33 188 ~~Cross correlation between registered image sets was performed using the e_correlate function within IDL~~
34
35 189 ~~version 7.0. Correlations were run within small sub-regions of the registered image volumes. In Fig. 1,3~~
36
37 190 ~~& 4, 50 μ m side cube sub-regions were manually defined by selecting volumes containing high contrast~~
38
39 191 ~~boundaries. For cross correlations between individual brains scanned for each transgenic line in ZBB (Fig~~
40
41 192 ~~2a,b), 40 μ m side cubes were drawn around the three computationally identified brightest sub-regions~~
42
43 193 ~~within the expression pattern, with cross correlation then calculated between all pairs of brains. The mean~~
44
45 194 ~~of all cross correlations was used to estimate registration precision.~~

46 195 Mean Landmark Distance (MLD). To assess registration precision using MLDs, corresponding landmarks
47
48 196 were located and annotated on the reference brain, and on unregistered brains. In each case, landmarks
49
50 197 were chosen to be widely distributed within the brain, and readily recognized in corresponding brain
51
52 198 scans. In addition, to verify recognizability, the *vglut2a* landmarks in the reference brain were located by
53
54 199 3 blinded scorers ; mean distance from each of the 10 reference points ranged from 1.7 to 11.8 μ m (mean,
55
56 200 4.5 \pm 0.9 μ m). Using ImageJ, we positioned a 3 micron cube centered on each landmark in a second
57
58 201 channel for each brain scan, then, after registering the brain scan using the first channel, applied the
59
60 202 resulting transformation matrix to the second channel, using Nearest Neighbor interpolation for both
61
62 203 CMTK and ANTs. Landmark distance was taken as the distance between the geometrical center of the
63
64 204 corresponding cubes in the reference image, and in the registered image.
65

Hausdorff distance. We manually segmented cells in a *vglut:DsRed* brain scan in a second channel and applied transformation matrices for registration to this second channel. Segmented cells were broadly distributed to ensure that distortion measures sampled the entire brain, and cell masks conservatively drawn within the boundaries of the soma. We then compared the morphology of cells after registration (A), to their original shape (B) by calculating the partial Hausdorff distance [30]. Briefly, for every point in a segmented cell mask before registration, we found the minimum distance to a point in the same mask after registration. The Hausdorff distance is the maximum of all such distances, calculated for both A→B and B→A. Because the Hausdorff distance is highly sensitive to cell alignment, and registration displaces cells from their original location, we found the optimal alignment for comparisons using a two-step process. First we aligned the geometric center of each cell in the original and transformed images. Second we searched for the minimal Hausdorff distance across 4940 rigid transformations of the aligned cell, within a 3 x 3 x 3 micron cube, (0.25 micron steps in each dimension). Finally, as Hausdorff distances are sensitive to outliers, we used the 95th percentile distances instead of the maximum Hausdorff distance for all measures [30].

Cell volume. For each segmented cell, we calculated its change in volume as the absolute value of the fractional change in the number of pixels after application of a transformation matrix.

Elongation index. For each pixel in a segmented cell, we found the maximal distance (MD) to any other pixel in the mask . The elongation index for a given cell was the 95th percentile largest value of MD, which we take as an approximation of the diameter of the cell across its longest axis.

Cross correlation. Cross correlation between the tERK-stained reference brain, and registered tERK stains, was performed using the `c correlate` function within IDL version 7.0. Correlations were run within eighteen 50 µm-side cube sub-regions of the image volumes that were manually selected to encompass high contrast boundaries and the mean of the 18 values taken as the mean cross correlation (MCC) for each brain in Fig. 3.

Jaccard index. Anti-tERK immunohistochemistry intensely stains tectal neuropil. Thus for measuring the accuracy of registration of the tectal neuropil, we manually segmented the left tectal neuropil area in 6 confocal scans of tERK stained larvae and our reference brain. We applied transformation matrices to these masks, then calculated the Jaccard index as the volume of the intersection between each registered mask (A) and the reference brain (B), divided by the total volume of the union of A and B.

Results

Optimization of ANTs based registration of live *vglut2a:dsRed-DsRed* image scans

1
2
3
4 239 Brain registration in Z-Brain and ZBB used the B-spline elastic transformation in CMTK. Before
5
6 240 attempting to co-align Z-Brain and ZBB, we tested an alternate algorithm for brain alignment, the
7
8 241 diffeomorphic symmetric normalization (SyN) method in ANTs, because: (1) SyN has been shown to
9
10 242 outperform B-spline transformations for deformable image registration in a variety of imaging modalities
11
12 243 [31,32]. (2) ANTs permits registration using multiple reference channels, potentially allowing the use of
13
14 244 multiple complementary expression patterns as references for improved registration fidelity. (3) By
15
16 245 calculating forward and reverse transformations simultaneously, SyN transformation matrices are
17
18 246 intrinsically symmetric, ensuring that bridging registrations would be unbiased and that we could easily
19
20 247 perform reciprocal transformations to register each dataset into the other's coordinate system.

21 249 To calibrate registration parameters, we assessed the alignment precision and distortion of cell
22
23 250 morphology after the registration of six representative *vglut2a:DsRed* scans to the original *vglut2a:DsRed*
24
25 251 reference brain in ZBB (*vglut2a_{ZBB}*; file *vglut-dsred-ref-01.nii.gz*, available from [33], procedure
26
27 252 summarized in Fig. 1a). Similar to CMTK we employed a three step registration within ANTs where rigid
28
29 253 and affine steps were used to initialize a deformable registration using the SyN diffeomorphic
30
31 254 transformation with cross correlation (CC) as the similarity metric. We tested a range of values for each
32
33 255 of the SyN parameters as well as the radius of the region used for cross correlation.

34 257 To measure registration precision, we visually located 10 point-based landmarks in the *vglut2a_{ZBB}* pattern
35
36 258 (Additional File 1a-c) and in each of the 6 *vglut2a:DsRed* confocal scans. We then used the *vglut:DsRed*
37
38 259 channel for registration, and applied the resulting transformation matrix to the landmarks in each of the 6
39
40 260 brains. We measured the distance of each landmark from its location in the *vglut2a_{ZBB}* reference brain
41
42 261 (Additional File 1a,d). We designated the average of the 10 distances the 'Mean Landmark Distance'
43
44 262 (MLD). To assess the amount of distortion in cell shapes produced by the parameter sets, we segmented
45
46 263 107 cells in an unregistered *vglut2a:DsRed* confocal scan (Additional File 2), and applied each
47
48 264 transformation matrix to this set of cell masks. Changes in cell shape were measured using the partial
49
50 265 Hausdorff distance for each cell after registration compared to its original shape (see Methods).

51 267 Next we plotted the MLD against the Hausdorff distance and located points along the Pareto frontier (Fig.
52
53 268 1b) of these two measures. These points represent potentially optimal transformations, where registration
54
55 269 accuracy can only be improved by increasing distortion, or vice versa. To distinguish between these
56
57 270 points, we examined two additional measures of distortion: the change in cell volume (Fig. 1c) and
58
59 271 maximal elongation (Fig. 1d). Three transformations showed statistically significantly reduced distortion
60
61 272 compared to CMTK for both measures, and we selected the one (Fig. 1b, point d) with the greatest

1
2
3
4
5
6
7
8
9
10
11
12
13
14
15
16
17
18
19
20
21
22
23
24
25
26
27
28
29
30
31
32
33
34
35
36
37
38
39
40
41
42
43
44
45
46
47
48
49
50
51
52
53
54
55
56
57
58
59
60
61
62
63
64
65

273 precision for further testing. With this set of parameters (see Table 1, **live registration**), mean registration
274 error was within the diameter of a single neuron for both ANTs and CMTK (MLD for ANTs 6.7 ± 0.3
275 μm , for CMTK $7.6 \pm 0.4 \mu\text{m}$; N = 6 brains, paired t-test $p=0.056$). However, cell morphology was better
276 preserved using ANTs (Hausdorff Distance for ANTs 2.30 ± 0.14 , CMTK 2.37 ± 0.14 ; N = 107 cells,
277 paired t-test $p=0.013$), especially within ventral structures such as the hypothalamus and the caudal
278 medulla oblongata (Fig. 1e).

279
280 We first calibrated registration conditions by assessing alignment precision for a representative
281 *vglut2a:DsRed* scan registered to the original *vglut2a:DsRed* reference brain in ZBB (*vglut2a_{ZBB}*; file
282 *vglut_dsred_ref_01.nii.gz*, available from [33]). Similar to CMTK we employed a three step registration
283 within ANTs where rigid and affine steps were used to initialize a deformable registration using the SyN
284 diffeomorphic transformation with cross correlation (CC) as the similarity metric. We tested a range of
285 values for each of the SyN parameters as well as the radius of the region used for cross correlation.

286
287 While we previously used brain wide normalized cross correlation (NCC) to evaluate registration [1],
288 correlation within local anatomical regions that contain discrete landmarks has been shown to be a more
289 reliable criterion for quantitatively assessing registration precision [34]. Accordingly, in this work we
290 quantified precision in two ways; by measuring local registration errors both computationally as well as
291 manually. For the computational measure, we identified a set of 12 landmarks within the *vglut2a* pattern,
292 each within a $50 \mu\text{m}$ side cube. Landmarks were broadly distributed in the hope of representing diverse
293 brain regions and minimizing the bias for any single structure. We measured the cross correlation
294 between the corresponding regions in *vglut2a_{ZBB}* and the registered image, then calculated the mean of the
295 cross correlation between all regions (MCC ; Fig. 1a). For the manual measure of precision, we identified
296 10 landmarks in the *vglut2a_{ZBB}* pattern that could be visually recognized (landmark positions are
297 described in Additional File 1), and calculated the mean landmark distance (MLD) from the
298 corresponding points in the registered image as assessed by three blinded experts. We also assessed the
299 results visually to subjectively assess the severity of tissue distortion. Unsurprisingly, similar to our
300 previous work with brain wide NCC, images with the highest MCCs generally showed more conspicuous
301 tissue distortion — thus although greater precision was achieved with increased deformation, we
302 preferred results where cell shape and axon tract morphology were preserved (Fig. 1b,c). Disregarding
303 parameter combinations that resulted in overt distortion, we identified a set of values (Table 1, **live**
304 **registration**) where cell morphology remained intact, but registration precision (MCC) was maximized.
305 With these parameters, although the MCC for *vglut2a* improved only slightly from 0.79 using CMTK to
306 0.81 using SyN, cell morphology was noticeably better preserved, especially within ventral structures

1
2
3
4 307 ~~such as the hypothalamus (Fig. 1d). Manual measurement of precision registration confirmed these~~
5
6 308 ~~findings: ANTs registration using values that avoided noticeable morphological distortion showed similar~~
7
8 309 ~~MLDs to images registered using CMTK (Table 2).~~

9 310
10
11 311 We next ~~tested~~examined whether these registration parameters also improved precision for the co-aligned
12
13 312 transgenic lines. For ZBB, we co-scanned transgene and enhancer trap expression patterns with the
14
15 313 *vglut2a:dsRed* transgene, allowing us to register each expression pattern to *vglut2a*_{ZBB}. We first compared
16
17 314 the overlap and morphology of the Mauthner cells from brain scans of three different individuals of
18
19 315 transgenic line *J1229aGt* [23]. Overlap of Mauthner cell bodies was similar for CMTK and ANTs (Fig.
20
21 316 ~~1e,f,g~~). However, in CMTK registered images, the Mauthner axon was distorted in the caudal medulla,
22
23 317 whereas axon morphology was preserved with ANTs. Second, in our previous work, we assessed the
24
25 318 precision of CMTK registration using line *y339Et* by independently scanning two sets of three larvae,
26
27 319 producing an average for each set, and visually comparing the result. With CMTK we had noted
28
29 320 misalignment of approximately 1 cell diameter in the neuropil of the optic tectum (Fig. 1hg). This was
30
31 321 substantially improved with ANTs, where there was much closer alignment of the two averages (Fig. 1ih).
32
33 322 ~~For quantification we calculated the cross correlation for 8 landmarks within the y339Et pattern, and~~
34
35 323 ~~found that the mean increased from 0.52 with CMTK to 0.63 with ANTs.~~

324 325 **Improved precision of ZBB after registration using ANTs**

326
327 ~~Based on the improved registration precision and reduced distortion of cell morphology achieved using~~
328 ~~SyN, w~~e next recompiled ZBB using ANTs for registration to create a more accurate atlas (unprocessed
329 ~~and registered brain images are available from [35]). We used~~ ANTs to register the entire set of 354 brain
330 scans from 109 different transgenic lines that were part of ZBB, then as before, averaged multiple larvae
331 to create a representation of each transgenic line, masked the average stacks to remove expression outside
332 the brain and re-imported the resulting images into our Brain Browser software. We refer to this new
333 recompilation of ~~our~~ the atlas as ZBB_{1,2}. Unprocessed and registered brain images are available online
334 [35].

335
336 ~~To determine whether ZBB_{1,2} was a quantitative improvement over ZBB, we calculated a cross-~~
337 ~~correlation score for each pattern in the browser. To avoid manually defining landmarks for each line, we~~
338 ~~instead computationally identified three regions inside each pattern with strong expression to serve as~~
339 ~~landmarks. For each of these regions, we iteratively performed pair-wise cross-correlations between all~~
340 ~~individual brains from the same transgenic line, allowing us to calculate a mean cross-correlation (MCC)~~

1
2
3
4 341 value for each line. We performed this procedure first for brains registered using CMTK, then for the
5 same set of brains registered using ANTs, allowing us to compare MCCs for the two methods (Fig. 2a).
6 342 Overall, the correlations increased slightly from ZBB to ZBB_{1,2} (0.32 ± 0.02 to 0.34 ± 0.02 ; paired t test
7 343 $p=0.15$). Although this was not statistically significant, it was instructive to examine instances with large
8 344 changes in mean cross correlation. Line y332Et labels a small set of cells with a salt and pepper pattern in
9 345 the right habenula. Here, cross correlation was greater after registration with CMTK (CMTK, 0.50;
10 346 ANTs 0.39), due at least in part to greater distortion of cells resulting in increased overlap between
11 347 individual fish despite the biological variability (Fig. 2b). In y341Et, distortion artifacts also appeared to
12 348 account for the large increase in MCC obtained with ANTs (CMTK, 0.19; ANTs 0.58). Here, cells in the
13 349 caudal hypothalamus had an elongated morphology after registration with CMTK, often stretching
14 350 outside the boundaries of the nucleus. Consequently, in this case distortion reduced rather than increased
15 351 the cross correlation score (Fig. 2c).

16 352 To determine whether ZBB_{1,2} was a quantitative improvement over ZBB, we identified two
17 353 conspicuously labeled cells or landmarks in each of 12 transgenic lines from the atlas (Additional File 3).
18 354 We marked these positions in each of the three brain scans for each line, then, after registration,
19 355 calculated the distance between corresponding points in each pair of brains. The mean of these distances
20 356 measures how precisely landmarks are registered across the three brains. We performed this procedure
21 357 first for brains registered using CMTK, then for the same set of brains registered using ANTs, allowing us
22 358 to compare MLDs for the two methods (Fig. 2a-b). Overall, landmark distances decreased from ZBB to
23 359 ZBB_{1,2} (10.8 ± 1.02 μm to 8.1 ± 0.83 μm ; $N = 24$ landmarks, paired t-test $p=0.008$), indicating that
24 360 ZBB_{1,2} has significantly improved precision, and confirming that the new atlas is accurate to
25 361 approximately the diameter of a single neuron. The improvement was greatest deeper in the brain (Fig. 2c
26 362 ; linear regression, $N=24$, $p=0.003$) with the largest improvement for the caudal hypothalamus in line
27 363 y341, where increased alignment precision was associated with noticeably reduced distortion between the
28 364 three brain scans (Fig. 2d).

29 365
30 366
31 367 Additionally, we inspected regions of ZBB_{1,2} where we had noticed poor registration precision or
32 368 pronounced cell distortion in the original ZBB. One such area was the dorsal thalamus, where cell
33 369 morphology was noticeably perturbed after elastic registration with CMTK, with cell somas stretching
34 370 across the midline (Fig. 2d2e). In ZBB_{1,2} cells retained a rounded morphology with distinct cell clusters
35 371 on the left and right sides of the brain (Fig. 2e2f). Similarly, distortions in cell shape that were apparent in
36 372 the caudal hypothalamus in ZBB, were absent in ZBB_{1,2} (Fig. 2f2g,gh). In the caudolateral medulla, we
37 373 previously obtained poor registration, with expression extending to regions outside the neural tube (Fig.
38 374 2h2i). In ZBB_{1,2}, patterns had improved bilateral symmetry and were correctly confined to the neural tube

1
2
3
4 375 (Fig. 2i2j). Finally, we noticed that the posterior commissure was poorly aligned between larvae leading
5
6 376 to a defasciculated appearance in ZBB (Fig. 2i2k), whereas this tract had the ~~correct expected~~ tightly
7
8 377 bundled appearance in ZBB_{1,2} (Fig. 2i2l).

9 378
10
11 379 Together, these observations confirm that ZBB_{1,2} is a more faithful representation of the transgenic lines.
12
13 380 Not only is cell morphology better preserved, but ~~metrics of~~ global registration precision ~~as measured by~~
14 381 ~~mean cross-correlation are nevertheless~~ improved ~~from those of~~ compared to the original ZBB atlas.
15
16 382

17 383 **Optimization of ANTs registration parameters for fixed tissue**

18
19 384
20
21 385 The Z-Brain atlas was derived by registering brain scans to a single brain that was fixed, permeabilized
22
23 386 and immunostained for tERK expression. We therefore ~~presumed anticipated~~ that tERK would be a useful
24
25 387 channel for bridging the two atlases, if we could first successfully register a tERK stained *vglut2a:DsRed*
26 388 expressing brain to ZBB_{1,2}. Therefore, we fixed and ~~eo~~-stained a transgenic *vglut2a:DsRed* larva for
27
28 389 ~~DsRed and~~ tERK, and registered the tERK pattern to ZBB_{1,2} using the *vglut2a* pattern. We used the
29
30 390 resulting image as our ZBB tERK reference brain (tERK_{ZBB}; file *terk-ref-02.nii.gz* available from [33]).
31 391

32
33 392 In addition to the tERK reference brain, Z-Brain contains an average tERK representation from 197
34
35 393 tERK stained larvae, which we thought might serve as a bridge between atlases. During studies on pERK-
36
37 394 based activity mapping, we had previously generated a dataset of 167 tERK stained brains and ~~sought to~~
38 395 ~~use therefore used~~ these to create ~~an our own~~ average tERK representation by registering them to
39
40 396 tERK_{ZBB}. However, during this process, we noticed a high degree of variability between tERK stained
41
42 397 brains, most salient notably in ~~either~~ poor labeling of ventral brain structures ~~and or~~ in deformation of the
43 398 optic tectum neuropil. Immunohistochemistry for tERK proved highly sensitive to staining parameters
44
45 399 with the trypsin activity, permeabilization duration, and antigen retrieval having the strongest effects. This
46 400 variability in fixed tissue was most apparent in the optic tectum, where high trypsin activity tended to
47
48 401 disrupt morphology and reduce the volume of the tectal neuropil (Fig. 3a3b, b-c). These local distortions
49
50 402 were not ~~corrected resolved~~ by deformable image registration: alignment to tERK_{ZBB} with the same
51
52 403 parameters optimized for live *vglut2a* based registration, failed to correct the reduced tectal neuropil
53
54 404 volume (Fig. 3e3d, d-e; asterisk) and often created an artifact where the neuropil zone failed to abut the
55
56 405 underlying cellular layer labeled by *vglut2a* expression (Fig. 3e3d, d-e; arrowheads).
57 406

1
2
3
4 407 We therefore varied the registration parameters that were optimal for live *vglut2a* registration, to find
5
6 408 settings that best rectified the variable tissue morphology following fixation and permeabilization
7
8 409 (process summarized in Fig. 3a).
9
10 410 For ~~tERK-optimization of fixed tissue registration-optimization~~, we used a set of 6 tERK stained brains
11 411 ~~(including the Z-Brain tERK reference).~~ We iteratively varied parameters for registration to tERK_{ZBB}
12 412 and calculated the mean cross-correlation between each of the aligned tERK stains and tERK_{ZBB} (e.g.,
13 413 Fig. 3e,f). Again when visually inspected, we noted a trade-off between the quality of global alignment
14 414 and local distortion artifacts, with the parameters which yielded the greatest increase in MCC often
15 415 producing abnormally elongated cell profiles throughout the brain (Fig. 3g). However, visual inspection
16 416 confirmed that parameters which increased MCC for fixed tissue greatly improved the morphology of the
17 417 optic tectum neuropil (Fig. 3h,i). We therefore used ANTs with the fixed brain parameters (Table 1, **fixed**
18 418 **registration**) to register 167 tERK stained brains to tERK_{ZBB}, and generated an average tERK
19 419 representation comparable to the Z-Brain tERK average (Fig. 3j,k). iteratively varied parameters for
20 420 registration to tERK_{ZBB} and assessed registration fidelity. For measuring precision, we were not able to
21 421 identify unambiguous landmarks within the optic tectum, so we instead calculated the cross-correlation
22 422 between each of the aligned tERK stains and tERK_{ZBB} within small volumes, including parts of the tectum
23 423 (Fig. 3f,g). To verify that the 'fixed brain' parameters that yielded the greatest cross correlation did in fact
24 424 improve registration within the tectum, we manually segmented the tectal neuropil in the same 6 brains,
25 425 applied the transformation matrix to each mask, and calculated the Jaccard index for overlap with the
26 426 segmented neuropil in tERK_{ZBB}. Parameters for fixed brain registration produced a significant increase in
27 427 overlap, compared to the live brain parameters (Fig. 3h,i) and visual inspection confirmed that the
28 428 morphology of the optic tectum neuropil after registration was greatly improved (Fig. 3j,k). We therefore
29 429 used ANTs with the fixed brain parameters (Table 1, **fixed registration**) to register our 167 tERK stained
30 430 brains to tERK_{ZBB}, and generated an average tERK representation comparable to the 197 tERK average in
31 431 Z-Brain (Fig. 3l,m).
32
33
34
35
36
37
38
39
40
41
42
43
44
45
46
47

48 433 **Inter-atlas registration using multi-channel diffeomorphic transformation**

49 434
50
51 435 ~~By chance, both~~ Z-Brain and ZBB incorporated ~~seven additional eight gene or transgene~~ expression
52 436 patterns that we judged ~~were~~ sufficiently similar to act either as templates for bridging the datasets and/or
53 437 to provide metrics for assessing the precision of a bridging registration (Table ~~32~~, Additional File 4). For
54 438 example, *vglut2a*_{ZBB} is a confocal scan of DsRed in a single larva from transgenic line
55
56
57 439 *TgBAC(slcl7a6b:loxP-DsRed-loxP-GFP)nns14*, whereas Z-Brain includes *Tg(slcl7a6:EGFP)zf139*. In
58
59 440 both cases, reporter expression is regulated by the same bacterial artificial chromosome [15,20]. Crossing
60
61
62
63
64
65

1
2
3
4 441 these two lines allowed us to scan DsRed and EGFP in the same larva and confirm that the patterns were
5
6 442 largely congruous, potentially allowing us to use *vglut2a* expression to bridge the two atlases. Likewise,
7
8 443 the expression patterns of *tERK*, *elavl3*, *isl2b*, *vmat2* in Z-Brain and ZBB appeared sufficiently similar to
9 444 provide templates for atlas co-registration.

10
11 445
12 446 ~~We used seven expression patterns to evaluate registration precision using cross-correlation: *vglut2a*,~~
13 447 ~~*isl2b*, *vmat2*, *elavl3*, *isl1*, *gad1b* and *glyT2*. For each pattern we identified a set of 5–18 landmarks that~~
14 447
15 448 ~~were widely distributed to represent diverse brain regions. For each landmark, we measured the cross-~~
16 448
17 449 ~~correlation between the corresponding volumes in ZBB and Z-Brain. We then calculated the mean of all~~
18 449
19 450 ~~cross-correlation (MCC) values for landmarks associated with a given expression pattern. We used two~~
20 450
21 451 ~~measures of registration precision. The first metric (M_1) was the mean of the MCCs for *isl1*, *gad1b* and~~
22 451
23 452 ~~*glyT2* expression patterns in ZBB and in Z-Brain after registration to ZBB. These three expression~~
24 452
25 453 ~~patterns do not provide sufficient coverage across all brain regions to use for registration, but served as~~
26 453
27 454 ~~independent channels to estimate registration precision. However, as these patterns are relatively sparse~~
28 454
29 455 ~~they do not comprehensively assess precision across all brain regions. To provide a global measure of~~
30 455
31 456 ~~precision, we therefore also used a second metric (M_2) that was the mean of all seven MCCs: those in M_1~~
32 456
33 457 ~~plus four of the patterns used as references for registration—*vglut2a*, *tERK*, *isl2b* and *vmat2*. Although M_2~~
34 457
35 458 ~~uses expression patterns that together provide good coverage for the entire brain, we expected that the~~
36 458
37 459 ~~four patterns that were also used to guide the deformable registration, would artificially inflate the MCC.~~

38 461 ~~We first used CMTK to register Z-Brain to ZBB_{1,2}. Maximal M_1 and M_2 scores were obtained using the~~
39 461
40 462 ~~average *vglut2a* pattern as the reference (Fig. 4a). We therefore registered all images in Z-Brain to ZBB~~
41 462
42 463 ~~using the *vglut2a* average in each dataset as the reference channel. We observed severe tissue distortions~~
43 463
44 464 ~~in several brain regions, with noticeable flattening of the torus longitudinalis and gross tissue distortions,~~
45 464
46 465 ~~particularly in ventral brain regions (Fig. 4b,c; ZBrain-CMTK).~~

47 466
48 467 ~~Next, for comparison, we used the ANTs SyN algorithm to register the atlases. Ideally, patterns for~~
49 467
50 468 ~~registration should include information throughout the brain. Because ANTs can use multiple concurrent~~
51 468
52 469 ~~reference channels to derive an optimal transformation matrix, we speculated that the best possible~~
53 469
54 470 ~~transformation would be achieved by a combination of channels with complementary information. We~~
55 470
56 471 ~~therefore produced an inter-atlas transformation matrix using every combination of the *elavl3*, *isl2b*,~~
57 471
58 472 ~~*vglut2a*, *vmat2*, *tERK_{REF}* (*tERK* single brain) and *tERK_{AV}* (*tERK* average brain) patterns as references. As~~
59 472
60 473 ~~Z-Brain used fixed samples, we used the registration parameters previously optimized for the greater~~
61 473
62 474 ~~variability present in fixed tissue. Multi-channel registration significantly improved M_1 and M_2 values~~

1
2
3
4 475 compared to any single channel alone and to transformations obtained using CMTK. The registration
5
6 476 obtained with *vglut2a*, *tERK_{REL}*, *vmat2* and *isl2b* gave the highest M_2 value and an M_1 score within 1% of
7
8 477 the highest scoring combination (Fig. 4a). Moreover, the overt tissue distortions noted after elastic
9
10 478 registration with CMTK were far less salient using these parameters (Fig. 4b,c ; ZBrain-SyN). This
11
12 479 conclusion was supported when we assessed registration precision by visually locating landmarks in the
13
14 480 *vglut2a* pattern after registration with CMTK, or multi-channel ANTs registration. After calculating the
15
16 481 distance from the same points in the *vglut2a_{ZBB}* pattern we found the multi-channel ANTs registered
17
18 482 points were on average 9.9 μm away from the reference points, compared to 17.9 μm for CMTK (Table
19
20 483 4). We therefore applied the transformation matrix obtained with this set of channels to the database of
21
22 484 gene expression patterns in Z-Brain to align them to *ZBB_{1,2}*.

23
24 485
25
26 486 The precision of the inter-atlas registration is apparent when comparing the location of cells that are
27
28 487 present in both datasets, such as those labeled by *Pet1:GFP*. The Z-Brain transformed pattern closely
29
30 488 matches the transgene expression pattern in *ZBB_{1,2}* within the superior raphe (Fig. 4d — note however
31
32 489 that unexpectedly, the line in *ZBB_{1,2}* also labels a set of more rostral cells not apparent in Z-Brain). Both
33
34 490 atlases also include lines labeling the Mauthner cells. After registration, Mauthner cells in the atlases
35
36 491 substantially overlapped, although they were several microns more medially positioned in *ZBB_{1,2}* (Fig.
37
38 492 4e). Similarly, we used the inverse of the transformation generated by SyN to register *ZBB_{1,2}* to the Z-
39
40 493 Brain coordinate system. As expected, expression in the *DAT:GFP* line in *ZBB_{1,2}* overlapped well with
41
42 494 the tyrosine hydroxylase stain from Z-Brain in the pretectum (Fig. 4f), although again, the *ZBB_{1,2}* pattern
43
44 495 was slightly more medial than in Z-Brain. More caudally, the *glyT2:GFP* transgenic line labels
45
46 496 glycinergic neurons in longitudinal columns in the medulla oblongata [36]. These columns were closely
47
48 497 aligned after *ZBB_{1,2}* was registered to Z-Brain (Fig. 4g). Although best practice is to align directly to
49
50 498 either *ZBB* or Z-Brain, because many researchers will have already registered data sets to either *ZBB* or
51
52 499 Z-Brain, or for cases where it may not be possible to directly register a dataset, we have provided
53
54 500 transformation matrixes and detailed instructions to quickly re-align datasets to either of the coordinate
55
56 501 systems ([37]; instructions are provided in Additional File 2).

57
58 502 Taking advantage of the ability of ANTs to use of multiple reference channels concurrently, we compared
59
60 503 the effect of combinatorial use of complementary reference channels for inter-atlas registration (process
61
62 504 summarized in Fig. 4a). We used seven expression patterns to evaluate registration precision: *vglut2a*,
63
64 505 *isl2b*, *vmat2*, *tERK*, *isl1*, *gad1b* and *glyT2*. For each pattern we identified a set of 4-10 point-based
65
66 506 landmarks that could be identified in corresponding *ZBB* and Z-Brain images and that were widely
67
68 507 distributed to represent diverse brain regions (total of 41 landmarks ; Additional File 5). We marked these
69
70 508 points in each set of images, registered Z-Brain images to *ZBB_{1,2}* images, measured the distance between

1
2
3
4 509 cognate landmarks and calculated the mean landmark distance for each of the seven expression patterns.
5
6 510 We used two summary measures of registration precision. The first metric (M_1) was the mean of MLDs
7
8 511 for the three patterns that were not used to drive registration (*isl1*, *gad1b* and *glyT2*). Although these
9
10 512 channels measure precision independent of the patterns for atlas registration, they are relatively sparse
11
12 513 and do not assess precision across the whole brain. Thus, to provide a global measure of precision, we
13
14 514 also used a second metric (M_2) that was the mean of all seven MLDs: those in M_1 plus four of the patterns
15
16 515 used as references for registration — *vglut2a*, tERK, *isl2b* and *vmat2*.

17
18 517 Using CMTK, minimal M_1 and M_2 scores were obtained using the average *vmat2* pattern as the reference
19
20 518 (Fig. 4b; mean MLD for 41 landmarks $14.9 \pm 1.3 \mu\text{m}$). We therefore registered all images in Z-Brain to
21
22 519 ZBB using the *vmat2* average in each dataset as the reference channel. We observed severe tissue
23
24 520 distortions in several brain regions, with noticeable flattening of the torus longitudinalis as well as gross
25
26 521 tissue distortions, particularly in ventral brain regions (Fig. 4c,d; ZBrain-CMTK). Next we used the
27
28 522 ANTs SyN algorithm to register the atlases. Ideally, patterns for registration should include information
29
30 523 throughout the brain. Because ANTs can use multiple concurrent reference channels to derive an optimal
31
32 524 transformation matrix, we speculated that the best possible transformation would be achieved by a
33
34 525 combination of channels with complementary information. We therefore produced an inter-atlas
35
36 526 transformation matrix for every combination of the *elavl3*, *isl2b*, *vglut2a_{AV}* (*vglut2a* average brain),
37
38 527 *vmat2*, tERK_{ZBB} (tERK single brain) and tERK_{AV} (tERK average brain) patterns as references. Because Z-
39
40 528 Brain used fixed samples, we used the registration parameters optimized for the greater variability present
41
42 529 in fixed tissue. Multi-channel registration significantly reduced M_1 and M_2 values compared to any single
43
44 530 channel alone and to transformations obtained using CMTK. The registration obtained with *vglut2a*,
45
46 531 tERK_{ZBB}, *vmat2* and *isl2b* gave the lowest global metric (M_2) value and an M_1 score within 10% of the
47
48 532 lowest scoring combination (Fig. 4b). With these parameters, the MLD was $9.1 \pm 0.8 \mu\text{m}$ (N=41
49
50 533 landmarks) and the overt tissue distortions noted after elastic registration were far less salient (Fig. 4c,d;
51
52 534 ZBrain-SyN). We therefore applied the transformation matrix obtained with this set of channels to the
53
54 535 database of gene expression patterns in Z-Brain to align them to ZBB_{1,2}, and used the inverse of the
55
56 536 transformation generated by SyN to register ZBB_{1,2} to the Z-Brain coordinate system. We imported all Z-
57
58 537 Brain expression patterns not previously represented in the database into ZBB_{1,2}, producing a total of 133
59
60 538 expression patterns.

61
62 539
63
64 540 The accuracy of the inter-atlas registration is evident when comparing the location of cells that are present
65
66 541 in both datasets, such as those labeled by *pet1:GFP*. The Z-Brain transformed pattern closely matches the
67
68 542 transgene expression pattern in ZBB_{1,2} within the superior raphe (Fig. 4e — note however that

1
2
3
4 543 [unexpectedly, the line in ZBB_{1.2} also labels a set of more rostral cells not apparent in Z-Brain](#)). Both
5
6 544 [atlases also include lines labeling the Mauthner cells. After registration, Mauthner cells in the atlases](#)
7
8 545 [substantially overlapped, although they were several microns more medially positioned in ZBB_{1.2} \(Fig.](#)
9
10 546 [4f\). Expression in the *DAT:GFP* line in ZBB_{1.2} overlapped well with the tyrosine hydroxylase stain from](#)
11
12 547 [Z-Brain in the pretectum \(Fig. 4g\), although again, the ZBB_{1.2} pattern was slightly more medial than in Z-](#)
13
14 548 [Brain. Caudally, the *glyT2:GFP* transgenic line labels glycinergic neurons in longitudinal columns in the](#)
15
16 549 [medulla oblongata \[36\]. These columns were closely aligned after ZBB_{1.2} was registered to Z-Brain \(Fig.](#)
17
18 550 [4h\).](#)

19 551
20 552 [Although best practice is to align directly to either ZBB or Z-Brain, because many researchers will have](#)
21
22 553 [already registered data sets to either ZBB or Z-Brain, or for cases where it may not be possible to directly](#)
23
24 554 [register a dataset, we have provided transformation matrixes and detailed instructions to quickly re-align](#)
25
26 555 [datasets to either of the coordinate systems \(\[37\]; Additional File 6\).](#)

27 556 28 557 [Neuroanatomical visualization](#)

29 558
30
31 559 Z-Brain includes 294 masks that represent anatomically defined brain regions or discrete clusters of cells
32
33 560 present in transgenic lines. We selected 113 of these masks that delineate neuroanatomical regions and
34
35 561 transformed them into the ZBB_{1.2} coordinate system. We had previously defined a small number of our
36
37 562 own anatomical masks by thresholding clusters of neuronal cell bodies located in well-defined brain
38
39 563 regions. ~~In contrast,~~ [However](#) the Z-Brain masks are more comprehensive, have smoother boundaries and
40
41 564 include both the cell bodies and neuropil for a given region (Fig. 4*h-k*). We therefore imported the Z-
42
43 565 Brain masks into ZBB_{1.2}, replacing most of our existing masks. We also modified the Brain Browser
44
45 566 software to automatically report the neuroanatomical identity of a selected pixel, or to display the
46
47 567 boundaries of the region encompassing a selected point. The updated software and rebuilt database in
48
49 568 ZBB_{1.2} can be downloaded from our website [38].

50 569
51 570 Finally, as the Zebrafish Brain Browser's strength is primarily in two dimensions (i.e., the visualization of
52
53 571 horizontal, transverse, and sagittal slices through the brain), we decided to develop interactive tools to
54
55 572 better facilitate ~~three-dimensional~~ [3D](#) exploration. The use of 3D graphics to represent complex structure
56
57 573 can also provide a more intuitive sensory experience that avoids cognitive bias or misinterpretation
58
59 574 inadvertently introduced by ~~sometimes largely arbitrary~~ two dimensional reductions [39,40]. By taking
60
61 575 advantage of stereoscopy and vestibular-enhanced parallax (head tracking), the more immersive and
62
63 576 holistic experience of Virtual Reality (VR) can also significantly improve performance of basic tasks like

1
2
3
4 577 searching and making comparisons [41,42]. We therefore implemented our Zebrafish Brain Browser in
5
6 578 both an open Web3D platform (X3D) and a custom game engine (Unity). First, we converted masks
7
8 579 representing anatomical regions to meshes and built a Web3D interface using X3D to inspect the spatial
9
10 580 relationship between different brain regions (Fig. 5a,b), [available online](#) [43]. Users can navigate within
11
12 581 the brain using any web browser, rotating and zooming into brain regions to better interrogate larval
13
14 582 neuroanatomy. Second, using the Unity platform we wrote a VR app to view the brain and
15
16 583 neuroanatomical regions. By running the app on a cell phone, and inserting it into an inexpensive Google
17
18 584 cardboard viewer, users can 'walk into' the brain, and see from the inside the inter-relationship between
19
20 585 neuroanatomical domains (Fig. 5c,d), [available for download](#) [44].
21 586

21 587 Discussion

22 588
23
24 589 Digitized data-derived brain atlases provide an opportunity to continuously integrate new information and
25
26 590 iteratively improve data accuracy within a common spatial framework. Thus, as methods evolve and
27
28 591 technology improves, new insights can be easily added to existing data to provide an increasingly rich
29
30 592 view of brain structure and function. Because the entire larval zebrafish brain can be rapidly imaged at
31
32 593 cellular resolution, it is possible to envisage an atlas that combines detailed information on cell type
33
34 594 (including gene expression and morphology), connectivity and activity under a variety of different
35
36 595 physiological conditions. At present, biological variability presents an obstacle, as brain regions contain
37
38 596 multiple intermingled cell types that are not positioned in precisely the same manner between larvae. To
39
40 597 ~~circumvent~~ [compensate for](#) this in the existing zebrafish brain atlases, multiple individuals of a given line
41
42 598 are sampled and averaged to generate a representative expression pattern. Current atlases are thus
43
44 599 essentially heat maps of gene expression or activity. Despite this spatial ambiguity, aggregating
45
46 600 information from different sources into the same spatial framework still provides valuable indicators of
47
48 601 cell type, gene co-expression, and neural activity under defined conditions.
49 602

49 603 Ideally different atlas projects might use the same reference brain, however in practice the choice of a
50
51 604 reference is [often](#) dictated by study-specific experimental requirements. For example, despite the
52
53 605 deformations introduced by fixation and permeabilization, a fixed brain is essential for activity mapping
54
55 606 using pERK immunohistochemistry. In contrast, we were able to take advantage of the optical
56
57 607 transparency of larvae to rapidly scan and register several hundred individuals representing more than 100
58
59 608 different transgenic lines. For our purposes, the *TgBAC(slc17a6b:loxP-DsRed-loxP-GFP)nns14* line was
60
61 609 ideal, because through Cre injection, we generated a *vglut2a:GFP* line with an almost identical pattern,
62
63 610 allowing us to co-register lines with either GFP or RFP fluorescence. However, we have also used pan-

1
2
3
4
5
6
7
8
9
10
11
12
13
14
15
16
17
18
19
20
21
22
23
24
25
26
27
28
29
30
31
32
33
34
35
36
37
38
39
40
41
42
43
44
45
46
47
48
49
50
51
52
53
54
55
56
57
58
59
60
61
62
63
64
65

611 neuronal Cerulean or mCardinal as a reference channel when ~~the~~ green and red channels both contained
612 useful information on transgene expression. Our work now demonstrates that it is feasible to contribute to
613 community efforts at building an integrated map of brain structure, expression and activity, while
614 allowing reference image selection to be guided by technical considerations.

615
616 One caveat to this conclusion is that deformable image registration can easily introduce artifacts into cell
617 morphology if parameters are not carefully monitored and constrained. Indeed, a special challenge for
618 brain registration in zebrafish is preserving the local morphology of neuronal cell bodies and axons, while
619 permitting sufficient deformation to correct for biological differences and changes in brain structure
620 arising from tissue fixation and permeabilization. Thus, while B-spline registration with CMTK produced
621 acceptable inter-atlas alignment, it also introduced noticeable distortions into local brain structure that
622 affected neuronal cell morphology. Such artifacts were particularly severe in ventral brain regions such as
623 the caudal hypothalamus, and may therefore be due to differences in ventral signal intensity between the
624 datasets. In ZBB, in order to compensate for the increase in light diffraction with tissue depth, we
625 systematically increased laser intensity with confocal scan progression (z-compensation). As a result, the
626 Z-Brain and ZBB datasets are comparable in dorsal brain regions, but there is a noticeable discrepancy
627 ventrally which may account for the loss of registration fidelity. Alternatively, although z-compensation
628 partially corrects for reduced fluorescent intensity, there is a noticeable drop-off in image resolution in
629 ventral regions; the resulting loss of information may lead to lower quality registration. Registration
630 algorithms that allow parameters to vary by depth may ameliorate the effects of these physical imaging
631 constraints.

632
633 Nevertheless, the symmetrical diffeomorphic transformation in ANTs provides a ~~satisfactory~~ solution to
634 these problems. For live tissue, we found parameters that allowed the ANTs SyN transform to achieve
635 similar or better registration precision than previously achieved using CMTK, while ~~minimizing~~
636 significantly reducing ~~overt~~ distortions in tissue structure and neuronal cell morphology. In our hands,
637 permeabilization of fixed tissue tended to produce variable changes in neuropil structure which was most
638 salient in the optic tectum. Specifically, neuropil volume was diminished when fresh aliquots of trypsin
639 were used for extended durations. These artifacts can be minimized by stringent oversight of reagent
640 viridity. However, by calibrating SyN parameters to permit larger deformations, we were able to
641 accommodate the variability introduced in tissue processing.

642
643 Currently, ~~the main~~ limitations ~~for use~~ of the SyN registration algorithm in ANTs are the large memory
644 demands (73 GB for a single channel registration) and long computational times (3-5 hours for a single

1
2
3
4 645 channel using 24 cores) required for registration of images with a resolution sufficient for the brain-wide
5
6 646 visualization of neuronal morphology (e.g., 1000 x 600 x 350 pixels). For multi-channel registrations,
7
8 647 memory demands and computation time were even greater: 106 GB for 6 channels taking over 16 hours
9
10 648 on 24 cores. However, our present ANTs SyN parameters likely can be further optimized to reduce these
11
12 649 demands. For instance, our parameters currently include 10 iterations of transformation matrix
13
14 650 optimization at full image resolution. From our experience, these full resolution registration cycles do not
15
16 651 significantly ~~improve cross-correlation scores~~increase precision, but greatly increase computation time.
17
18 652 Thus, computation time may be reduced by adjusting registration resolution as well as other parameters
19
20 653 without adversely affecting registration quality. Although computational resources did not present a
21
22 654 bottleneck for registering a small number of samples, this increase in the demands of a single registration
23
24 655 made it difficult to optimize registration parameters as extensively as we had done previously with
25
26 656 CMTK [1]. ~~For example, during our initial effort to optimize registration parameters for live *vglut2a*~~
27
28 657 ~~expression, we used a single representative example rather than assessing parameters for a set of several~~
29
30 658 ~~independent scans.~~By reducing computation time, we would be able to explore more comprehensively
31
32 659 the parameter space available with SyN and evaluate alternative diffeomorphic transforms available with
33
34 660 ANTs that may provide still better registration fidelity.

35
36 661
37
38 662 An obstacle to systematically calibrating registration parameters ~~was~~is finding a suitable metric to
39
40 663 quantitatively evaluate ~~registration~~ precision. This is a recognized problem, and it is not clear that a
41
42 664 general solution exists [34]. Here, we primarily assessed precision by measuring the distance between
43
44 665 visually-located landmarks in the reference brain, and registered images. However, this method has two
45
46 666 drawbacks: (1) it relies on the accuracy with which these landmarks are located, and (2) at least for our
47
48 667 sample set, a relatively limited set of landmarks could reliably be identified. We obtained similar results
49
50 668 when we assessed precision using ~~We used~~ cross-correlation within localized image neighborhoods that
51
52 669 included ~~relatively~~ high contrast internal image boundaries (data not shown). ~~However~~ in registering live
53
54 670 *vglut2a:DsRed* image stacks, we ~~found that the highest scoring transformations achieved~~noted the trade-
55
56 671 off between accurate global brain alignment and at the expense of biologically plausible cell morphology.
57
58 672 Thus we also used a set of measures to assess changes in the morphology of manually segmented cells
59
60 673 (Hausdorff distance, elongation index and cell volume). Finally, we also ~~Therefore, it was essential to~~
61
62 674 visually compare ~~inspected~~ the output of every transformation and make subjective judgments about
63
64 675 subjectively judge registration quality. ~~This was difficult, because distortions, when present, tended to be~~
65
66 676 ~~variable in different parts of the image, thus requiring the entire image stack produced by each~~
67
68 677 ~~transformation to be scrutinized to select optimal parameter settings.~~

1
2
3
4 679 ~~Nevertheless,~~ This study demonstrates that the ANTs diffeomorphic symmetric normalization algorithm
5
6 680 ~~(SyN) improves advances~~ upon elastic registration for precise registration of whole brain images in larval
7
8 681 zebrafish and is markedly better at preserving neuronal cell morphology. By systematically testing SyN
9
10 682 registration parameters for registering images acquired using live scans, we improved the ZBB atlas.
11
12 683 Then, after calibrating registration parameters for fixed tissue and using multi-channel optimization, we
13
14 684 were able to align the Z-Brain atlas into the ZBB coordinate space, and vice-versa, [achieving co-](#)
15
16 685 [registration accuracy to approximately the diameter of a single neuron](#). We believe that integrating the
17
18 686 information present in each of these atlases produces a richer framework for future studies of structural
19
20 687 and functional relationships within the nervous system. Large digital datasets such as those present in
21
22 688 brain atlases can be used for many types of bioinformatic analysis. Z-Brain and ZBB already include
23
24 689 software that can be used to explore the larval zebrafish brain, and we hope that ~~by~~ integrating these
25
26 690 datasets into a single coordinate system, ~~we~~ will help to stimulate the development of additional
27
28 691 computational tools and methods for querying this information.

692 693 **Availability of supporting data**

694
695 All individual brain scans, both before and after registration to a ZBB reference brain, are available in the
696 *GigaScience* repository, GigaDB [35]. The GigaDB repository also includes the set of reference brains
697 used for ZBB [33] and the transformation matrices used to convert between ZBB and Z-Brain coordinate
698 systems [37].

699 700 **Abbreviations**

701
702 ac, anterior commissure
703 [Ce, cerebellum](#)
704 DT, Thalamus
705 GT, Griseum tectale
706 Ha, Habenula
707 Hc, Hypothalamus caudal zone
708 Hi, Hypothalamus intermediate zone
709 MO, Medulla oblongata
710 NXm, Vagus motor neurons
711 OB, Olfactory bulb
712 OE, Olfactory epithelium
713 [ON, Olfactory nerve](#)
714 IO, Inferior olive
715 LC, Locus coeruleus
716 MN, Mauthner neuron
717 MO, Medulla oblongata
718 Pal, Pallium

1
2
3
4 719 pc, posterior commissure
5 720 [Po, preoptic region](#)
6 721 Pr, Pretectum
7 722 SR, Superior raphe
8 723 Teg, Tegmentum
9 724 TeOn, Optic tectum neuropil
10 725 TG, Trigeminal ganglion
11 726 TL, Torus longitudinalis
12 727 [TS, Torus semicircularis](#)
13 728
14
15

16 729
17
18 730 **Competing Interests**

19 731
20
21 732 The authors declare that they have no competing interests.
22
23 733

24 734 **Authors' Contribution**

25 735
26 736 GDM and HAB conceived the experiments. GDM, KMT, EJH and HAB optimized ANTS for zebrafish
27 737 brain registration. GDM, MB and AKG contributed confocal brain scans and generated meshes. NFP
28 738 developed the X3D/HTML5 based browser. DDN developed the Unity VR browser. GDM and HAB
29 739 wrote the manuscript. All authors approved the final manuscript.
30
31
32
33

34 740
35
36 741 **Acknowledgements**

37 742
38 743 This work was supported by the Intramural Research Program of the *Eunice Kennedy Shriver* National
39 744 Institute for Child Health and Human Development (NICHD) and utilized the high-performance
40 745 computational capabilities of the Biowulf Linux cluster at the National Institutes of Health, Bethesda, MD
41 746 [45]. We thank Owen Randlett for valuable discussion and help checking the correspondence of *vglut2a*
42 747 expression patterns. We are grateful to Sinisa Pajevic (NIH/CIT) for advice on computational procedures
43 748 and to M. Okan Irfanglu and Neda Sadeghi (NICHD) for guidance in optimizing ANTs parameters.
44
45
46
47
48
49
50

51 750 **References**

52 751
53 752 1. Marquart GD, Tabor KM, Brown M, *et al.* A 3D Searchable Database of Transgenic Zebrafish Gal4
54 753 and Cre Lines for Functional Neuroanatomy Studies. *Front Neural Circuits* 2015; **9**:78.
55
56 754 2. Randlett O, Wee CL, Naumann EA, *et al.* Whole-brain activity mapping onto a zebrafish brain atlas.
57 755 *Nat Methods* 2015; **12**:1039–1046.
58
59
60
61
62
63
64
65

- 1
2
3
4 756 3. Ronneberger O, Liu K, Rath M, *et al.* ViBE-Z: a framework for 3D virtual colocalization analysis in
5 757 zebrafish larval brains. *Nat Methods* 2012; **9**:735–42.
- 6
7 758 4. Rath M, Nitschke R, Filippi A, Ronneberger O, Driever W. Generation of high quality multi-view
8
9 759 confocal 3D datasets of zebrafish larval brains suitable for analysis using Virtual Brain Explorer (ViBE-
10 760 Z) software. *Protoc Exch* 2012.
- 11
12 761 5. Portugues R, Feierstein CE, Engert F, Orger MB. Whole-Brain Activity Maps Reveal Stereotyped,
13 762 Distributed Networks for Visuomotor Behavior. *Neuron* 2014; **81**:1328–1343.
- 14
15 763 6. Rohlfing T, Maurer CR Jr. Nonrigid image registration in shared-memory multiprocessor environments
16 764 with application to brains, breasts, and bees. *IEEE Trans Inf Technol Biomed* 2003; **7**:16–25.
- 17
18 765 7. Avants BB, Epstein CL, Grossman M, Gee JC. Symmetric diffeomorphic image registration with
19 766 cross-correlation: Evaluating automated labeling of elderly and neurodegenerative brain. *Med Image Anal*
20 767 2008; **12**:26–41.
- 21
22
23 768 8. Avants BB, Tustison NJ, Song G, Cook PA, Klein A, Gee JC. A reproducible evaluation of ANTs
24 769 similarity metric performance in brain image registration. *NeuroImage* 2011; **54**:2033–2044.
- 25
26 770 9. Higashijima S, Hotta Y, Okamoto H. Visualization of cranial motor neurons in live transgenic
27 771 zebrafish expressing green fluorescent protein under the control of the islet-1 promoter/enhancer. *J*
28 772 *Neurosci* 2000; **20**:206–18.
- 29
30 773 10. Wen L, Wei W, Gu W, *et al.* Visualization of monoaminergic neurons and neurotoxicity of MPTP in
31 774 live transgenic zebrafish. *Dev Biol* 2008; **314**:84–92.
- 32
33
34 775 11. Xi Y, Yu M, Godoy R, Hatch G, Poitras L, Ekker M. Transgenic zebrafish expressing green
35 776 fluorescent protein in dopaminergic neurons of the ventral diencephalon. *Dev Dyn* 2011; **240**:2539–47.
- 36
37 777 12. Lillesaar C, Stigloher C, Tannhauser B, Wullmann MF, Bally-Cuif L. Axonal projections originating
38 778 from raphe serotonergic neurons in the developing and adult zebrafish, *Danio rerio*, using transgenics to
39 779 visualize raphe-specific *pet1* expression. *J Comp Neurol* 2009; **512**:158–82.
- 40
41 780 13. Tabor KM, Bergeron SA, Horstick EJ, *et al.* Direct activation of the Mauthner cell by electric field
42 781 pulses drives ultra-rapid escape responses. *J Neurophysiol* 2014; **112**:834–844.
- 43
44
45 782 14. Scott EK, Baier H. The cellular architecture of the larval zebrafish tectum, as revealed by *gal4*
46 783 enhancer trap lines. *Front Neural Circuits* 2009; **3**:13.
- 47
48 784 15. Satou C, Kimura Y, Hirata H, Suster ML, Kawakami K, Higashijima S. Transgenic tools to
49 785 characterize neuronal properties of discrete populations of zebrafish neurons. *Development* 2013;
50 786 **140**:3927–31.
- 51
52
53 787 16. McLean DL, Fan J, Higashijima S, Hale ME, Fetcho JR. A topographic map of recruitment in spinal
54 788 cord. *Nature* 2007; **446**:71–5.
- 55
56 789 17. Pittman AJ, Law MY, Chien CB. Pathfinding in a large vertebrate axon tract: isotopic interactions
57 790 guide retinotectal axons at multiple choice points. *Development* 2008; **135**:2865–71.

1
2
3
4 791 18. Yokogawa T, Hannan MC, Burgess HA. The dorsal raphe modulates sensory responsiveness during
5 792 arousal in zebrafish. *J Neurosci* 2012; **32**:15205–15215.
6
7 793 19. Satou C, Kimura Y, Higashijima S. Generation of multiple classes of V0 neurons in zebrafish spinal
8 794 cord: progenitor heterogeneity and temporal control of neuronal diversity. *J Neurosci* 2012; **32**:1771–83.
9
10 795 20. Bae YK, Kani S, Shimizu T, *et al.* Anatomy of zebrafish cerebellum and screen for mutations
11 796 affecting its development. *Dev Biol* 2009; **330**:406–26.
12
13 797 21. Fosque BF, Sun Y, Dana H, *et al.* Labeling of active neural circuits in vivo with designed calcium
14 798 integrators. *Science* 2015; **347**:755–760.
15
16 799 22. Nechiporuk A, Linbo T, Poss KD, Raible DW. Specification of epibranchial placodes in zebrafish.
17 800 *Development* 2007; **134**:611–623.
18
19 801 23. Burgess HA, Johnson SL, Granato M. Unidirectional startle responses and disrupted left-right co-
20 802 ordination of motor behaviors in robo3 mutant zebrafish. *Genes Brain Behav* 2009; **8**:500–11.
21
22 803 24. Inoue D, Wittbrodt J. One for All—A Highly Efficient and Versatile Method for Fluorescent
23 804 Immunostaining in Fish Embryos. *PLOS ONE* 2011; **6**:e19713.
24
25 805 25. Schneider CA, Rasband WS, Eliceiri KW. NIH Image to ImageJ: 25 years of image analysis. *Nat*
26 806 *Methods* 2012; **9**:671–675.
27
28 807 26. Williams G. *NifTi Input/Output*. <https://imagej.nih.gov/ij/plugins/nifti.html> (last accessed, 22 March
29 808 2017)
30
31 809 27. Heisenberg M, Schmid B. *IntSeg 3D*. http://3dviewer.neurofly.de/IntSeg_3D (last accessed, 22 March
32 810 2017)
33
34 811 28. Web3D Consortium. *Open Standards for Real-Time 3D Communication*. <http://www.web3d.org/> (last
35 812 accessed, 22 March 2017)
36
37 813 29. Vicomtech-IK4. *AtlasConversionScripts*. <https://github.com/VolumeRC/AtlasConversionScripts> (last
38 814 accessed, 22 March 2017)
39
40 815 30. Huttenlocher DP, Klanderman GA, Rucklidge WJ. Comparing images using the Hausdorff distance.
41 816 *IEEE Trans Pattern Anal Mach Intell* 1993; **15**:850–863.
42
43 817 31. Klein A, Andersson J, Ardekani BA, *et al.* Evaluation of 14 nonlinear deformation algorithms applied
44 818 to human brain MRI registration. *NeuroImage* 2009; **46**:786–802.
45
46 819 32. Murphy K, Ginneken B van, Reinhardt JM, *et al.* Evaluation of Registration Methods on Thoracic
47 820 CT: The EMPIRE10 Challenge. *IEEE Trans Med Imaging* 2011; **30**:1901–1920.
48
49 821 33. *ZBB Reference Brains*. http://helix.nih.gov/~BurgessLab/reference_brains.zip (last accessed, 22 March
50 822 2017) To be replaced with GigaDB DOI upon publication
51
52 823 34. Rohlfing T. Image Similarity and Tissue Overlaps as Surrogates for Image Registration Accuracy:
53 824 Widely Used but Unreliable. *IEEE Trans Med Imaging* 2012; **31**:153–163.
54
55 825 35. *ZBB Raw and Registered Brain Images* GigaDB DOI to be provided upon publication
56
57
58
59
60
61
62
63
64
65

1
2
3
4
5
6
7
8
9
10
11
12
13
14
15
16
17
18
19
20
21
22
23
24
25
26
27
28
29
30
31
32
33
34
35
36
37
38
39
40
41
42
43
44
45
46
47
48
49
50
51
52
53
54
55
56
57
58
59
60
61
62
63
64
65

826 36. Kinkhabwala A, Riley M, Koyama M, *et al.* A structural and functional ground plan for neurons in the
827 hindbrain of zebrafish. *Proc Natl Acad Sci U A* 2011; **108**:1164–9.

828 37. *ZBB-ZBrain Transformation Matrices*. <https://helix.nih.gov/~BurgessLab/zbb-zbrain.zip> (last
829 accessed, 22 March 2017) To be replaced with GigaDB DOI upon publication

830 38. *Zebrafish Brain Browser*.<https://science.nichd.nih.gov/confluence/display/burgess/Brain+Browser>
831 (last accessed, 22 March 2017)

832 39. Ota D, Loftin B, Saito T, Lea R, Keller J. Virtual reality in surgical education. *Comput Biol Med*
833 1995; **25**:127–137.

834 40. Ware C, Franck G. Viewing a graph in a virtual reality display is three times as good as a 2D diagram.
835 In: *Proceedings of 1994 IEEE Symposium on Visual Languages*.; 1994:182–183.

836 41. Bowman DA, McMahan RP. Virtual Reality: How Much Immersion Is Enough? *Computer* 2007;
837 **40**:36–43.

838 42. Henry JAG, Polys NF. The effects of immersion and navigation on the acquisition of spatial
839 knowledge of abstract data networks. *Procedia Comput Sci* 2010; **1**:1737–1746.

840 43. *Zebrafish Anatomy Explorer*.
841 <http://metagrid2.sv.vt.edu/~npolys/NIH/Burgess/ZebraFishBrowser/ZebrafishBrowser.html> (last
842 accessed, 22 March 2017)

843 44. *Virtual reality brain browser*.
844 <https://science.nichd.nih.gov/confluence/display/burgess/Brain+Browser#BrainBrowser-vrfishbrain> (last
845 accessed, 22 March 2017)

846 45. *High Performance Computing at the NIH. 2016*. <https://hpc.nih.gov> (last accessed, 22 March 2017)

847
848 **Figure legends**

849
850 **Table 1. ANTs command parameters for image registration**

851
852 ~~**Table 2. Registration precision for CMTK, ANTs (using parameters for optimal mean cross**~~
853 ~~**correlation), and ANTs (using parameters that minimize distortion), as measured by manually**~~
854 ~~**locating landmarks within the image.**~~

855 ~~Values are distances in microns from the corresponding landmarks in the reference brain. Three experts~~
856 ~~located, blind to the identity of the samples, located the landmarks in each registered image. The distance~~
857 ~~shown is the mean of the three distances from the same landmarks in the reference brain. To assess~~
858 ~~reproducibility of locating landmarks in the reference brain, the same three people also located the~~
859 ~~landmarks in the reference brain (fourth column) demonstrating that these landmarks can be located by~~
860 ~~experts to within 5 microns.~~

Table 32. Brain images in ZBB and Z-Brain that were used as templates for registration and/or for measurement of registration precision.

Table 4. Precision of ZBB and Z-brain co-alignment after using CMTK with tERK as the registration channel, CMTK with *vglut2a:dsRed* as the registration channel or multi-channel registration using ANTs.

Distances (in microns) were measured as in Table 2, by three experts who were blind to the identity of the samples.

Figure 1. Optimization of parameters for registration of live brain scans using ANTs

(a) Overview of parameter optimization for live brain scans using ANTs. A calibration set of 6 *vglut2a:DsRed* confocal stacks with 10 point-based landmarks and 107 cell masks were registered to the *vglut2a_{ZBB}* reference with the same 10 point-based landmarks defined (left). MLDs for landmarks and Hausdorff distance for transformed cell masks compared to their originals were measured for each parameter set (middle). Optimal parameters selected from these metrics (b-d) were used to re-register all lines generating ZBB_{1,2} where MLD was measured from 2 additional landmarks in each of 12 co-aligned patterns (right). (a) Dorsal maximum projections through the twelve 50 x 50 x 50 μm cubes used to calculate the mean cross correlation (MCC) for *vglut2a* expression patterns. Top row shows projections for the reference image, *vglut2a_{ZBB}*, and bottom row shows projections for a representative *vglut2a:dsRed* brain that was registered to the reference brain using CMTK. Correlation coefficients are indicated in the bottom row. For this example, the MCC is the mean of the indicated values, 0.73.

(b) Hausdorff distance for cell shape comparison plotted against MLD for 68 sets of parameters tested using ANTs (grey and blue circles) and after registration using CMTK (orange). Blue circles labeled a-f indicate the Pareto frontier.

(c) Mean absolute change in cell volume (as a fraction of the original volume) produced by transformations resulting from parameter sets a-f and CMTK in (b). * $p < 0.05$, compared to CMTK.

(d) Mean elongation index for cells after registration using parameter sets a-f and CMTK in (b). Dashed line shows index for cells before registration — all transformations produced a significant increase in compared to the untransformed cells. * $p < 0.05$, compared to CMTK.

(b-de) Comparison of a single plane Horizontal section through the medulla oblongata in *vglut2a_{ZBB}*, and of the a representative *vglut2a:dsRed* brain after registration using CMTK or ANTs with parameters that produced the largest mean cross correlation score (0.85 ; MCC optimal), and ANTs with parameters where visual inspection showed cell morphology was best preserved (Visual optimal. MCC was 0.81).

1
2
3
4 895 ~~Slices are through the optic tectum (b), medulla oblongata (e) and hypothalamus (d).~~ Distortion artifacts
5
6 896 ~~introduced by CMTK in the hypothalamus (arrowhead) as well as poor cell morphology with CMTK and~~
7
8 897 ~~ANTs MCC optimal (arrow) are indicated (arrow).~~ Scale bar 50 μm
9
10 898 ~~(ef,fg)~~ Comparison of a single hHorizontal sectionplane in *J1229aGt* showing expression of GFP in the
11 899 Mauthner cell and axon (arrowheads) for three individual larvae (pseudo-colored red, green and blue).
12
13 900 Registration was performed with CMTK (ef) or ANTs (fg). Scale bar 100 μm.
14 901 ~~(gh,hi)~~ Single coronal plane-Transverse section through the optic tectum in two separate average brain
15 902 images (colored green and magenta) for *y393Et*. For each brain image, we independently scanned three
16 903 individual brains and registered them using CMTK (gh) or ANTs (hi). Scale bar 100 μm.
17
18 904
19
20
21 905 **Figure 2. Improved precision of transgene representations in ZBB_{1,2}**
22
23 906
24 907 ~~(a) Mean landmark distances for 24 landmarks~~~~Mean of cross-correlation values derived from all pairwise~~
25 ~~comparisons of individual brains for each transgenic line in ZBB~~, after registration with CMTK and
26 908 ANTs. Dotted line indicates 1:1 ratio.
27
28 909
29 910 ~~(b) Horizontal slice through the right habenula in y332Et, showing three individual brain scans after~~
30 ~~registration with CMTK (top row), and the same slices pseudo-colored (red, green blue) and~~
31 911 ~~superimposed. Bottom row shows the equivalent after registration using ANTs.~~
32
33 912
34 913 (b) Boxplot of data in (a). * paired t-test, N=12 lines, p = 0.019
35
36 914 (c) Difference in MLD between ANTs and CMTK plotted against distance from the dorsal-most point in
37 the brain.
38 915
39 916 ~~(ed)~~ Horizontal slice-section through the caudal hypothalamus of three individual *y341Et* larvae as well as
40 their pseudo-colored superimposition following registration with CMTK (top row) or ANTs (bottom
41 917 row).
42
43 918
44 919 ~~(de,ef)~~ Horizontal slice-section through the thalamus showing the averaged representation of enhancer
45 trap line *y304Et*, where individual brains were registered with CMTK for ZBB (de), or ~~with~~ ANTs for
46 920 ZBB_{1,2} (ef). Arrow indicates neurons that are artificially elongated across the midline. Scale bar 100 μm.
47
48 921 ~~(fg,gh)~~ Coronal slice-Transverse section through the caudal hypothalamus showing the average enhancer
49 922 trap line *y269Et* brain registered with CMTK (dg) ~~and~~ or with ANTs (eh). Arrow shows distortion of
50 923 cells causing the caudal hypothalamus to appear dorsally elongated. Scale bar 50 μm.
51 924
52
53 925 ~~(hi,ij)~~ Coronal slice-Transverse section through the medulla oblongata showing the average *phox2b:GFP*
54 926 brain with CMTK (fi) ~~and~~ or ANTs (gi). Scale bar 50 μm.
55
56 927 ~~(jk,kl)~~ Horizontal projection through the posterior commissure (arrow) for the average *y351Et* brain
57
58 928 obtained with CMTK (jk) or ANTs (kl). Scale bar 100 μm.
59
60
61
62
63
64
65

Figure 3. Optimization of ANTs registration parameters for fixed tissue

(a) Overview of parameter optimization for fixed brain scans using ANTs. A calibration set of 6 tERK confocal stacks with segmentations of the tectal neuropil were registered to tERK_{ZBB}, a tERK and *vglut2a:DsRed* confocal scan previously aligned to the *vglut2a_{ZBB}* reference (**left**). MCCs were calculated between eighteen 50 μm -side cube high-contrast sub-regions in the calibration set and in the tERK_{ZBB} reference to identify parameters that maximized MCC (**f,g**) and improved the Jaccard index of tectal neuropil segmentation (**h**) while compensating for fixation artifacts (**c,e,k**) (**middle**). These optimized ANTs parameters allow for the accurate registration of fixed tissue and the generation of a tERK average reference (tERK_{AV}) useful for bridging live and fixed tissue registrations (**right**).

(ab,bc) Horizontal section through the optic tectum after of tERK immunostaining for tERK (red) and *DsRed* in *vglut2a:DsRed* (green) larvae, using diluted (**ab**, sample A) or fresh trypsin (**bc**, sample B). Asterisk indicates missing area of tectal neuropil due to permeabilization artifact.

(ed,de) Horizontal section through the same stacks as in Registration, using the *vglut2a:DsRed* expression pattern, of the tERK immunostain (red) in same brains as in (**ab,bc**) registered to tERK_{ZBB} using the parameters previously optimized for live registration. White-Gray shows the ZBB_{1.2} *vglut2a:dsRed* pattern. Arrowheads highlight regions where tERK in the optic tectum neuropil fails to closely abut the adjacent glutamatergic cellular layer.

(ef) Mean-cross-correlation values MCC for the tERK expression pattern after registration of 6 brains to tERK_{ZBB}, varying each of the parameters for the ANTs SyN transform, starting with the parameters that gave the best registration for live *vglut2a:dsRed* based registration (SyN_#[0.05,6,0.5]). Bottom right: MCCs after varying the radius of the cross-correlation metric used during registration.

(fg) MCCs for tERK in the same brains as in (**ef**), after combining the two best parameter sets from (**ef**) (SyN[0.1,6,0.5] and SyN_#[0.05,6,0]) to assess further improvement in registration precision. Yellow box highlights the final optimal parameter set.

(g) Horizontal section for comparison of tERK stain revealing cell morphology in the pallium after registration with optimal parameters for live *vglut2a* registration (left), and optimal parameters for registering fixed and stained tissue (right).

(h) Jaccard index for overlap of the manually segmented tectal neuropil of the reference brain, with each of the 6 brains in the calibration set. $p < 0.01$

(i) 3D view of overlap between segmented tectal neuropils from tERK_{ZBB} (red) and the Z-Brain tERK reference brain (green), after registration with ANTs using parameter optimal for live registration, fixed registration and CMTK.

1
2
3
4 962 (**h,i,j,k**) Same brains as in (**e,d,e**), but after registration to tERK_{ZBB} using the parameters optimized for
5
6 963 fixed tissue registration.

7
8 964 (**j,k,l,m**) Horizontal section through the optic tectum showing tERK expression (red) and *vglut2a*:~~#D~~sRed
9
10 965 expression (green) in ZBB_{1,2} (**j,l**) and Z-Brain (**k,m**). Matching slices within the optic tectum were
11 966 selected; because the rotation around the y-axis is slightly different, sections are different within the
12
13 967 medulla.

14 968
15
16 969
17
18 970

19 971 **Figure 4. Transformation between Z-Brain and ZBB coordinate systems using multi-channel**
20
21 972 **registration**

22
23 973 [\(a\) Overview of bridging Z-Brain and ZBB using ANTs multi-channel registration. Combinations of 5](#)
24 974 [patterns common between Z-Brain and ZBB \(*vglut2a*_{AV}, tERK_{ZBB}, *vmat2*, *isl2b* and *elavl3*\) were used](#)
25
26 975 [guide multi-channel bridging registrations \(left\). MLDs for 41 landmarks in *gad1b*, *glyT2*, *isl1*, *isl2b*,](#)
27
28 976 [tERK, *vglut2a*, and *vmat2* expression were measured for all reference channel combinations \(middle\).](#)
29 977 [The combination of *vglut2a*_{AV}, tERK_{ZBB}, *vmat2*, and *isl2b* enabled the most accurate bridging of ZBB and](#)
30
31 978 [Z-Brain allowing the combination of the large collection of live transgenic lines of ZBB with the fixed](#)
32
33 979 [tissue techniques and expert neuroanatomic segmentations of Z-Brain \(right\).](#)

34 980 **(ab)** [MCC-MLDs](#) for the expression patterns of *gad1b*, *glyT2*, *isl1*, *isl2b*, ~~tERK_{ZBB}~~tERK, *vglut2a* and
35
36 981 *vmat2* and ~~the metrics~~ M₁ and M₂ [metrics](#); after registration of Z-Brain to ZBB_{1,2} using either CMTK or
37
38 982 ANTs SyN with fixed-tissue registration parameters and the indicated combination of reference channels
39
40 983 (*vglut2a*, tERK_{ZBBREF}, *vmat2*, *isl2b*, and *elavl3*). Note, similar results were obtained using ~~the~~ tERK_{AV}
41 984 instead of the tERK_{ZBBREF} ~~channel~~, but are omitted for clarity. The combination of reference channels
42
43 985 selected for co-registration of Z-Brain and ZBB is highlighted.

44 986 **(bc)** Transverse [view-section](#) through the caudal optic tectum showing the *vglut2a* pattern in ZBB_{1,2}, Z-
45
46 987 Brain, Z-Brain after registration to ZBB with CMTK (Z-Brain-CMTK), or with ANTs (Z-Brain-SyN).
47
48 988 The torus longitudinalis (TL) is well separated from tectal neurons in live scans, but less so in fixed tissue
49
50 989 (arrows). The TL appears flattened after CMTK registration, but retains normal morphology after
51
52 990 registration with ANTs SyN.

53 991 **(ed)** ~~A comparison of t~~ Transverse [views-sections](#) as in **(bc)**, but slightly more caudal with contrast
54
55 992 increased to highlight ventral distortion artifacts produced by registration (arrowheads).

56 993 **(de-gh)** Brain Browser views in the ZBB_{1,2} coordinate (**de,f**) or Z-Brain coordinate (**fg,h**) space. Scale
57
58 994 bars 25 μm except 50 μm in **(e)**

1
2
3
4 995 (de) Horizontal (top) and sagittal (bottom) [slices](#) sections, comparing the *Ppet1:GFP* expression pattern in
5
6 996 the superior raphe in ZBB_{1,2} (red) and Z-Brain after transformation to the ZBB coordinate system (green).
7
8 997 (ef) Horizontal (top) and [transverse coronal](#)-(bottom) [slices](#) sections through the medulla oblongata,
9
10 998 showing the expression of *y264Et* from ZBB_{1,2} (red) and *s1181Et* from [Z-Brain after transformation to](#)
11 999 [ZBB_{1,2} transformed Z-Brain](#) (green), which both label the Mauthner cells (arrowhead).
12
13 1000 (fg) Horizontal (top) and [transverse coronal](#)-(bottom) [slice](#) sections through the pretectum, comparing the
14 1001 expression of *DAT:GFP* from ZBB_{1,2} after transformation to Z-Brain [coordinates](#) (red) and anti-tyrosine
15
16 1002 hydroxylase staining in Z-Brain (green).
17
18 1003 (gh) Horizontal (top) and [transverse coronal](#)-(bottom) [slice](#) sections through the medulla oblongata for
19 1004 *glyT2:GFP* from ZBB_{1,2} after transformation to Z-Brain (red) and the same transgenic line in Z-Brain
20
21 1005 ([redgreen](#)).
22
23 1006 (hi-kl) Brain Browser horizontal [slices](#) sections showing manually segmented regions transformed from
24 1007 the Z-Brain coordinate system to ZBB_{1,2} (white outlines) compared to regions previously defined in ZBB
25
26 1008 obtained by thresholding expression patterns in transgenic lines (magenta). Regions are the torus
27
28 1009 longitudinalis ([hi](#)), habenula ([ij](#)), anterior commissure ([jk](#)) and trigeminal ganglion ([kl](#)).
29
30 1010

Figure 5. 3D visualization of brain browser data

31 1011
32
33 1012 (a) X3D zebrafish brain shown in HTML5 Web browser and (b) Virginia Tech HyperCube (CAVE)
34 1013 (c) Virtual reality brain rendered using the Unity Game Engine for stereoscopic viewing using the Google
35
36 1014 [e](#)Cardboard viewer. (d) In the VR browser, brain regions are selected using a menu on the floor of the
37
38 1015 virtual arena.

Additional Material

Additional File 1.pdf

Point-based landmarks for ~~manual~~ quantification of [live-scan](#) registration precision.

46 1020
47
48 1021 (a) Landmarks used for ~~manually~~ measuring registration precision. Position specifies the coordinates on
49
50 1022 *vglut2a*_{ZBB} (transverse, [sagittal](#), horizontal, ~~sagittal~~ planes). View indicates whether the image plane
51 1023 shown in (b) is or transverse (T), horizontal (H), or sagittal (S). [MLDs represent the average precision for](#)
52
53 1024 [each landmark for the set of 6 calibration brains, after registration with CMTK or ANTs.](#)
54
55 1025 (b) Images of the landmarks in *vglut2a*_{ZBB} (red) used for measuring precision [superimposed on elavl3](#)
56 1026 [\(gray\)](#).
57
58 1027 (c) Position of the landmarks superimposed on [horizontal dorsal](#)-(top) and sagittal (bottom) maximum
59 1028 projections of *elavl3* through the [larval](#) brain.

1
2
3
4 1029 [\(d\) Horizontal maximum projections showing the landmark point \(red dot\), and the position of the](#)
5
6 1030 [corresponding landmarks in the six calibration brains after registration \(green dots\) superimposed on](#)
7
8 1031 [*vglut2^α_{ZBB}*. Scale bar 20 μm.](#)

9 1032
10
11 1033
12
13 1034 [**Additional File 2.pdf**](#)

14 1035 [**Cells segmented for assessing distortion introduced by registration**](#)

15
16 1036 [\(a\) Position of manually segmented cells for measurement of distortion introduced by registration. Views](#)
17
18 1037 [show the same cells \(individually color coded\) superimposed on horizontal \(top\) and sagittal \(bottom\)](#)
19 1038 [maximum *elavl3* brain projections.](#)

20
21 1039 [\(b\) Two examples of cells showing \(left to right\): original confocal image, segmentation mask, mask after](#)
22
23 1040 [alignment with CMTK, and mask after alignment with ANTs.](#)

24 1041
25
26 1042 [**Additional File 3.pdf**](#)

27
28 1043 [**Point-based landmarks labeled by transgenic lines**](#)

29 1044 [\(a\) Transgenic line landmarks used for measuring registration precision of the zebrafish brain browser](#)
30
31 1045 [atlas. Coordinates give the transverse, horizontal, sagittal position. Letter in square brackets designates](#)
32
33 1046 [Right side \[R\], Left side \[L\], or Midline \[M\]. The mean and standard error of the landmark distances for](#)
34 1047 [the three brains per landmark are indicated for CMTK and ANTs.](#)

35
36 1048 [\(b\) Position of the landmarks superimposed on horizontal \(top\) and sagittal \(bottom\) maximum *elavl3*](#)
37
38 1049 [brain projections.](#)

39 1050
40
41 1051 [**Additional File 4.pdf**](#)

42
43 1052 [**ZBB and Z-Brain expression patterns used for atlas registration**](#)

44 1053 [Brain Browser 3D projections of corresponding expression patterns in Z-Brain \(left\) and ZBB \(right\) used](#)
45
46 1054 [for calibrating and verifying the precision of inter-atlas registration. The top 5 patterns were](#)
47
48 1055 [combinatorially used to drive registration, while the bottom 3 were used for assessing precision. Middle](#)
49 1056 [images show Z-Brain patterns after registration to ZBB.](#)

50
51 1057
52
53 1058 [**Additional File 5.pdf**](#)

54 1059 [**Point-based landmarks for measuring precision of Z-Brain/ZBB co-registration**](#)

55
56 1060 [\(a\) Transgenic line and tERK-stain landmarks used for measuring registration precision of registration](#)
57
58 1061 [between Z-Brain and ZBB. Coordinates are in transverse, horizontal, sagittal sections. Letters in square](#)
59 1062 [brackets designates Right side \[R\], Left side \[L\], or Midline \[M\]. Color blocks correspond to points in \(b\).](#)

1
2
3
4
5
6
7
8
9
10
11
12
13
14
15
16
17
18
19
20
21
22
23
24
25
26
27
28
29
30
31
32
33
34
35
36
37
38
39
40
41
42
43
44
45
46
47
48
49
50
51
52
53
54
55
56
57
58
59
60
61
62
63
64
65

[\(b\) Position of the landmarks superimposed on horizontal \(top\) and sagittal \(bottom\) maximum brain projections.](#)

Additional File [26.doc](#)

Instructions for using transformation matrices to convert between ZBB and Z-Brain coordinate systems.

Method	Step	Function	Command
Live Registration	1	Register vglut2a pattern in fish1-01.nii.gz, to the reference brain ref/vglut-ref.nii	antsRegistration -d 3 --float 1 -o [fish1_fish1_Warped.nii.gz] --interpolation WelchWindowedSinc --use-histogram-matching 0 -r [ref/vglut-ref.nii,fish1-01.nii.gz,1] -t rigid[0.1] -m MI[ref/vglut-ref.nii,fish1-01.nii.gz,1,32,Regular,0.25] -c [200x200x200x0,1e-8,10] --shrink-factors 12x8x4x2 --smoothing-sigmas 4x3x2x1vox -t Affine[0.1] -m MI[ref/vglut-ref.nii,fish1-01.nii.gz,1,32,Regular,0.25] -c [200x200x200x0,1e-8,10] --shrink-factors 12x8x4x2 --smoothing-sigmas 4x3x2x1vox -t SyN[0.05,6,0.5] -m CC[ref/vglut-ref.nii,fish1-01.nii.gz,1,2] -c [200x200x200x200x10,1e-7,10] --shrink-factors 12x8x4x2x1 --smoothing-sigmas 4x3x2x1x0vox
	2	Apply transformation matrix from (1) to a second channel for fish 1, in file fish1-02.nii.gz	antsApplyTransforms -d 3 -v 0 --float -n WelchWindowedSinc -i fish1-02.nii.gz -r ref/vglut-ref.nii -o fish1-02_Warped.nii -t fish1_1Warp.nii.gz -t fish1_0GenericAffine.mat
Fixed registration	1	Register tERK pattern in fish1-01.nii.gz, to the reference brain ref/terk-ref.nii	antsRegistration -d 3 --float 1 -o [fish1_fish1_Warped.nii.gz] --interpolation WelchWindowedSinc --use-histogram-matching 0 -r [ref/terk-ref.nii,fish1-01.nii.gz,1] -t rigid[0.1] -m MI[ref/terk-ref.nii,fish1-01.nii.gz,1,32,Regular,0.25] -c [200x200x200x0,1e-8,10] --shrink-factors 12x8x4x2 --smoothing-sigmas 4x3x2x1vox -t Affine[0.1] -m MI[ref/terk-ref.nii,fish1-01.nii.gz,1,32,Regular,0.25] -c [200x200x200x0,1e-8,10] --shrink-factors 12x8x4x2 --smoothing-sigmas 4x3x2x1vox -t SyN[0.1,6,0] -m CC[ref/terk-ref.nii,fish1-01.nii.gz,1,2] -c [200x200x200x200x10,1e-7,10] --shrink-factors 12x8x4x2x1 --smoothing-sigmas 4x3x2x1x0vox
	2	Apply transformation matrix from (1) to a second channel for fish 1, in file fish1-02.nii.gz	antsApplyTransforms -d 3 -v 0 --float -n WelchWindowedSinc -i fish1-02.nii.gz -r ref/terk-ref.nii -o fish1-02_Warped.nii -t fish1_1Warp.nii.gz -t fish1_0GenericAffine.mat

Table 1

ZBB			Z-Brain		Registration channel?	Quantification metric?
<i>Tg(vGlut2a:DsRed)nns14</i>	mean of 346 brains	↔	<i>Tg(vGlut2a:EGFP)zf139</i>	mean of 15 brains	y	y
<i>Tg(vGlut2a:DsRed)nns14</i>	single reference brain	↔	<i>Tg(vGlut2a:EGFP)zf139</i>	mean of 15 brains	y	n
<i>Tg(elavl3:CaMPARI)jf9</i>	mean of 3 brains	↔	<i>Tg(elavl3:GCaMP5G)a4598</i>	mean of 7 brains	y	n
<i>Tg(vmat2:GFP)pk2</i>	mean of 3 brains	↔	<i>Tg(vmat2:GFP)pk2</i>	mean of 55 brains	y	y
<i>Tg(isl2b:GFP)zc7</i>	mean of 3 brains	↔	<i>Tg(isl2b:Gal4)zc60</i>	mean of 8 brains	y	y
<i>tERK immunostain</i>	mean of 167 brains	↔	<i>tERK immunostain</i>	mean of 197 brains	y	y
<i>tERK immunostain</i>	single brain	↔	<i>tERK immunostain</i>	single reference brain	y	n
<i>Tg(isl1:GFP)rw0</i>	mean of 3 brains	↔	<i>Tg(isl1:GFP)rw0</i>	mean of 17 brains	n	y
<i>TgBAC(gad1b:GFP)nns25</i>	mean of 4 brains	↔	<i>TgBAC(gad1b:GFP)nns25</i>	mean of 10 brains	n	y
<i>Tg(glyT2:GFP)cf3</i>	mean of 6 brains	↔	<i>Tg(glyT2:GFP)cf3</i>	mean of 13 brains	n	y

Table 2

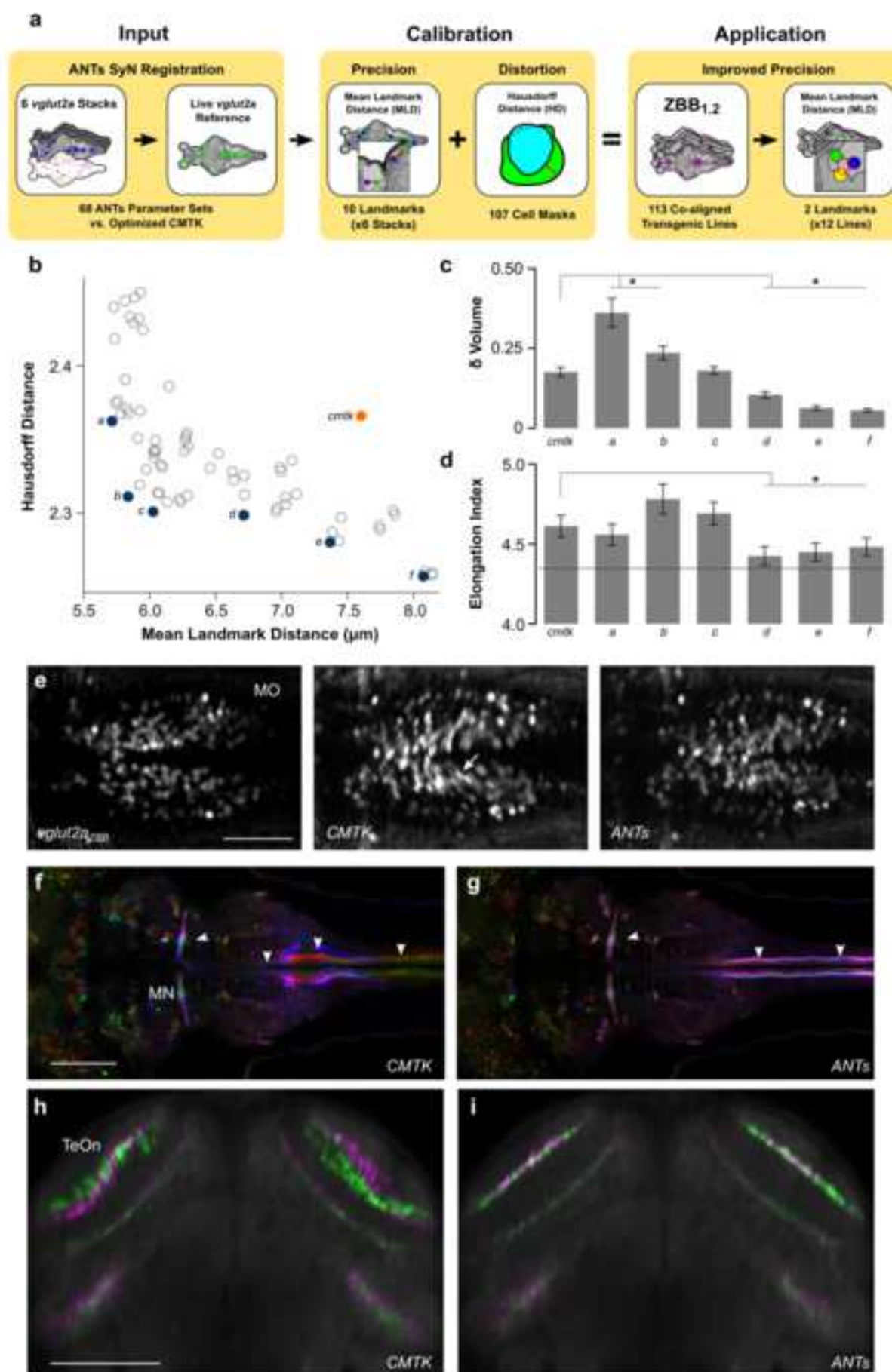


Figure 1

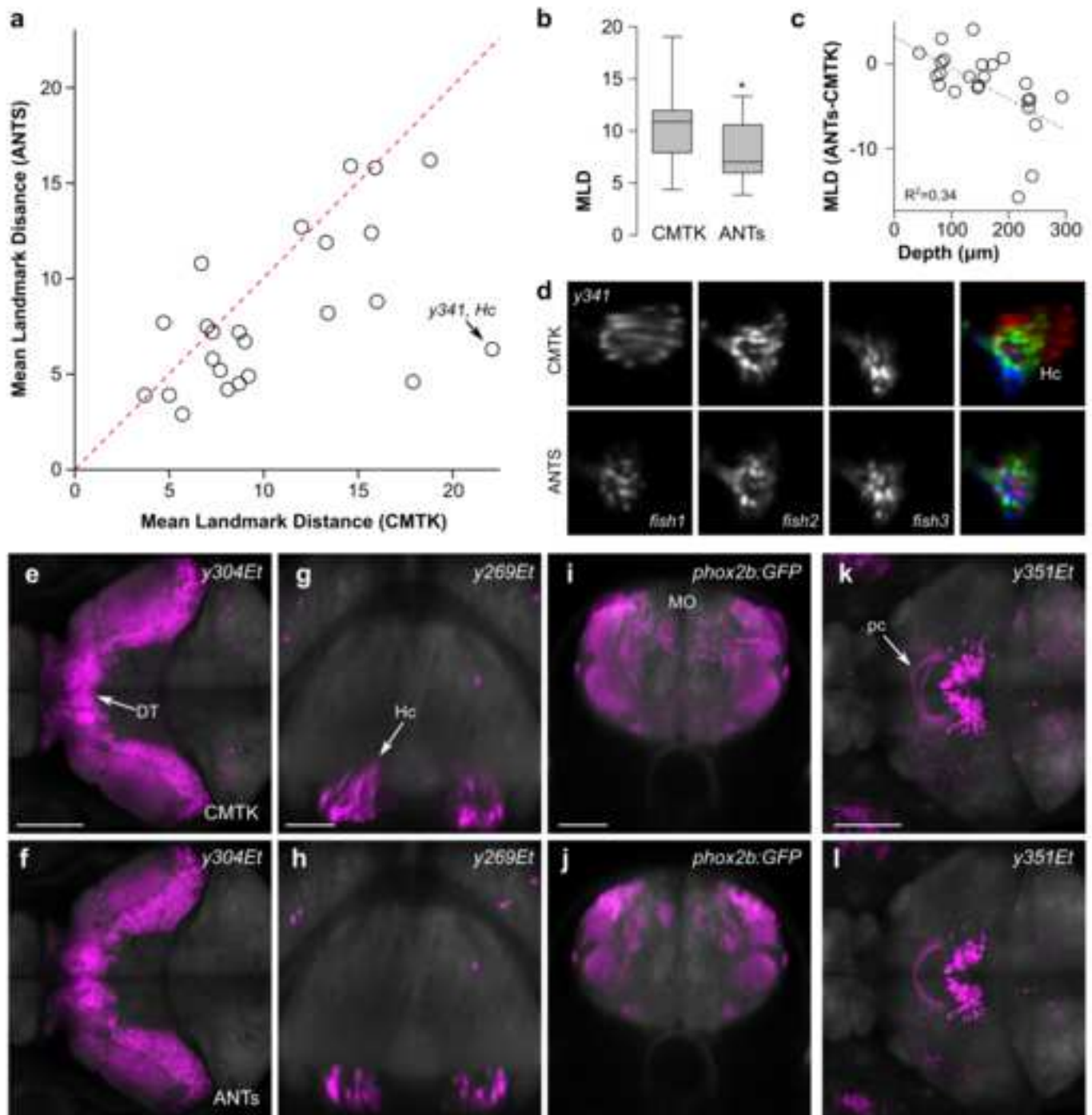


Figure 2

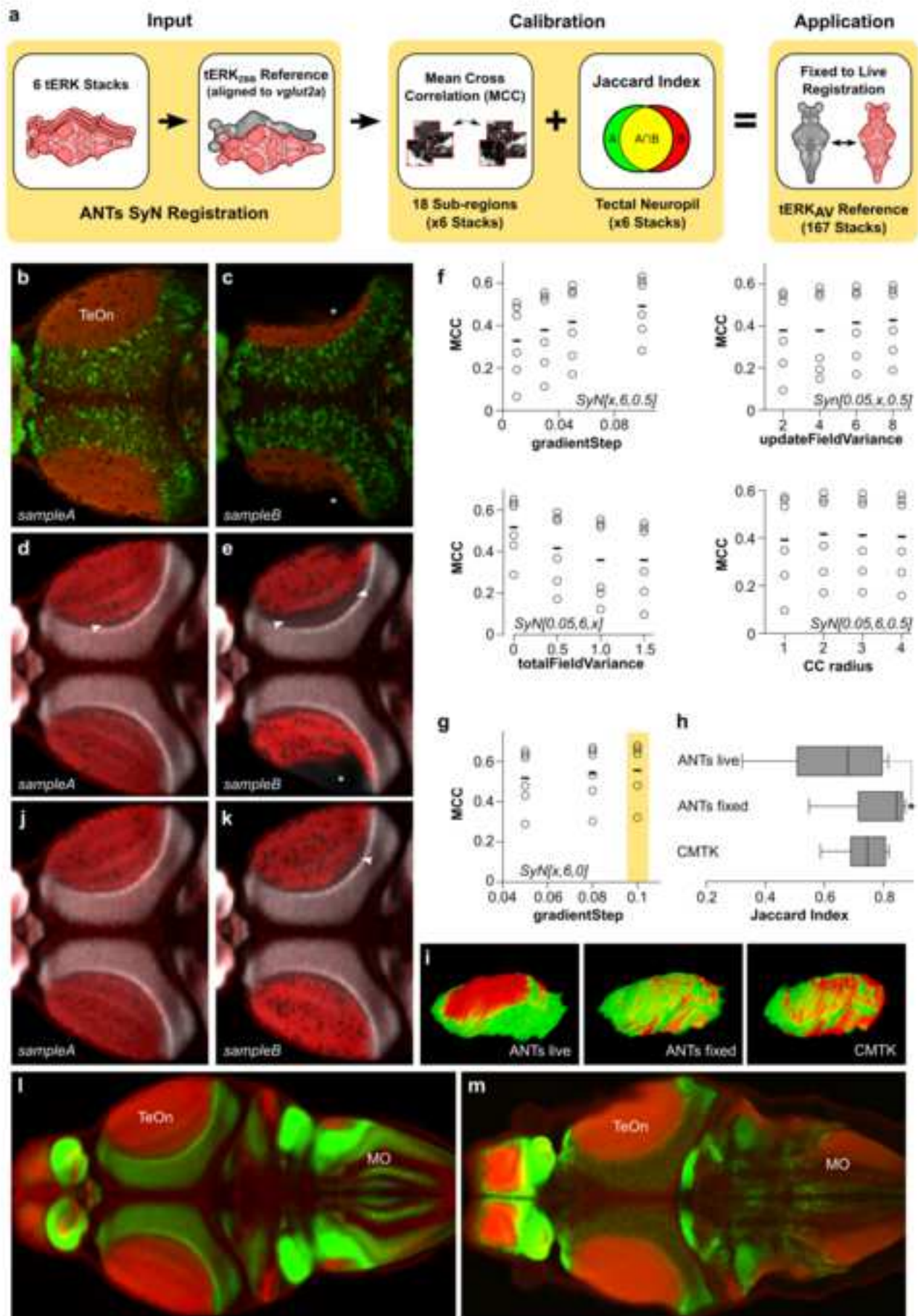


Figure 3

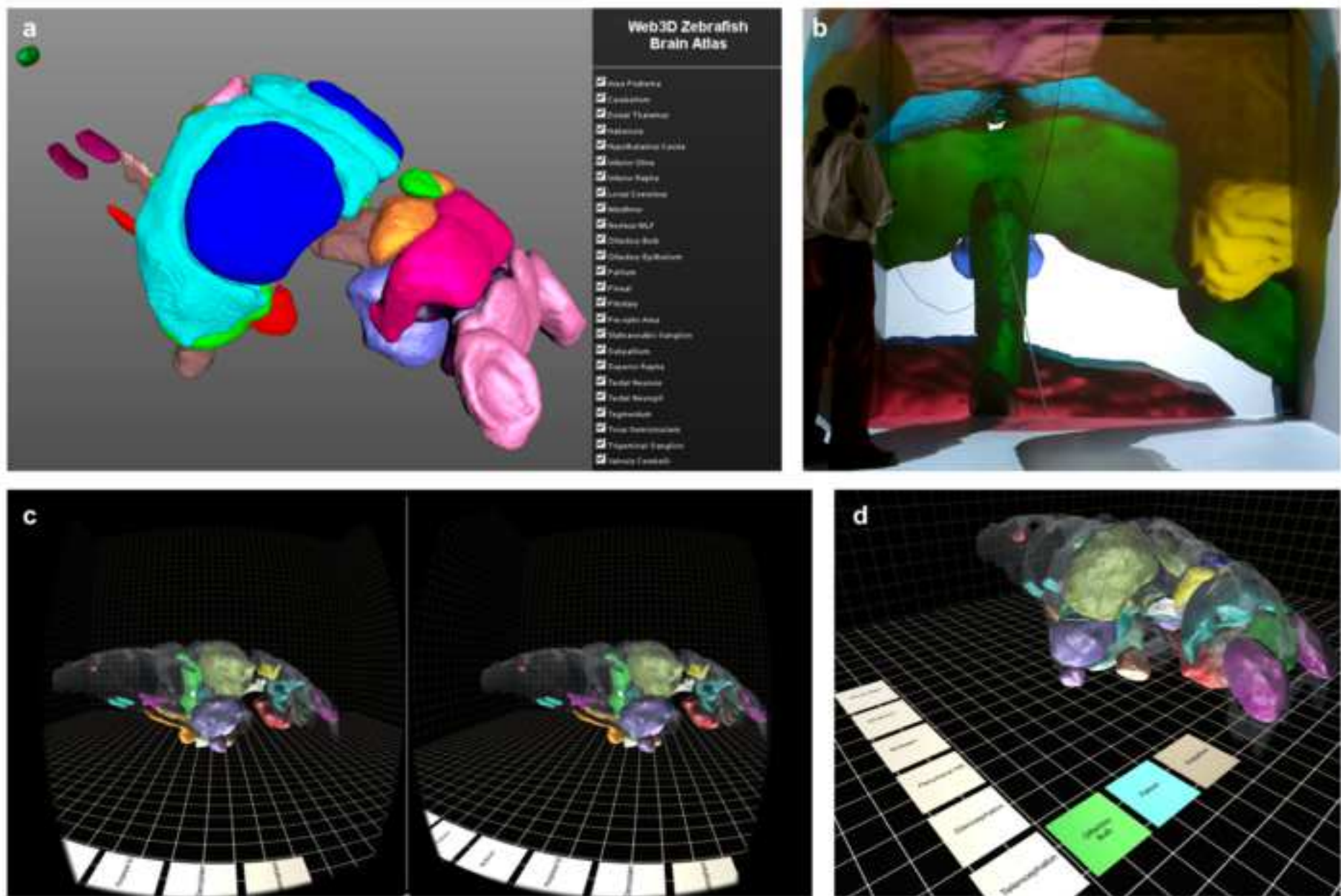
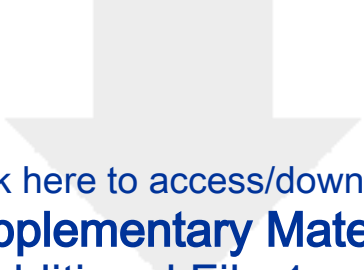
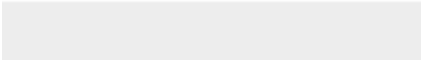



Figure 5





Click here to access/download
Supplementary Material
Additional File 1.png



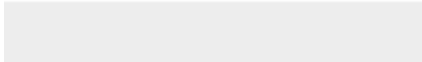


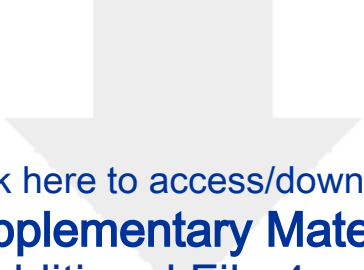
Click here to access/download
Supplementary Material
Additional File 2.png



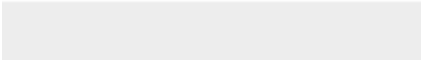


Click here to access/download
Supplementary Material
Additional File 3.png



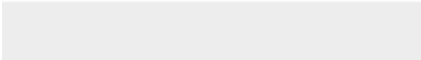



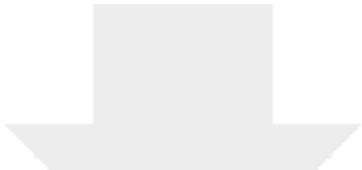
Click here to access/download
Supplementary Material
Additional File 4.png





Click here to access/download
Supplementary Material
Additional File 5.png





Click here to access/download
Supplementary Material
Additional File 6.docx

